Delaunay Tessellation Field Estimator analysis of the PSCz local Universe

Romano-Diaz, Emilio; van de Weygaert, Rien

Published in:
Monthly Notices of the Royal Astronomical Society

DOI:
10.1111/j.1365-2966.2007.12190.x

Publication date:
2007

Mon. Not. R. Astron. Soc. **382,** 2–28 (2007) doi:10.1111/j.1365-2966.2007.12190.x

Delaunay Tessellation Field Estimator analysis of the PSC*z* local Universe: density field and cosmic flow

Emilio Romano-Díaz[1,2,3]★ and Rien van de Weygaert[1]★

[1]*Kapteyn Astronomical Institute, University of Groningen, PO Box 800, 9700 AV, Groningen, the Netherlands*
[2]*Racah Institute of Physics, Hebrew University, Jerusalem 91904, Israel*
[3]*Department of Physics and Astronomy, University of Kentucky, Lexington, KY 40506-0055, USA*

Accepted 2007 July 5. Received 2007 June 19; in original form 2006 December 20

ABSTRACT

We apply the Delaunay Tessellation Field Estimator (DTFE) to reconstruct and analyse the matter distribution and cosmic velocity flows in the local Universe on the basis of the PSC*z* galaxy survey. The prime objective of this study is the production of optimal resolution 3D maps of the volume-weighted velocity and density fields throughout the nearby universe, the basis for a detailed study of the structure and dynamics of the cosmic web at each level probed by underlying galaxy sample. Fully volume-covering 3D maps of the density and (volume-weighted) velocity fields in the cosmic vicinity, out to a distance of $150\,h^{-1}$ Mpc, are presented. Based on the Voronoi and Delaunay tessellation defined by the spatial galaxy sample, DTFE involves the estimate of density values on the basis of the volume of the related Delaunay tetrahedra and the subsequent use of the Delaunay tessellation as natural multidimensional (linear) interpolation grid for the corresponding density and velocity fields throughout the sample volume. The linearized model of the spatial galaxy distribution and the corresponding peculiar velocities of the PSC*z* galaxy sample, produced by Branchini et al., forms the input sample for the DTFE study. The DTFE maps reproduce the high-density supercluster regions in optimal detail, both their internal structure as well as their elongated or flattened shape. The corresponding velocity flows trace the bulk and shear flows marking the region extending from the Pisces–Perseus supercluster, via the Local Superclusters, towards the Hydra–Centaurus and the Shapley concentration. The most outstanding and unique feature of the DTFE maps is the sharply defined radial outflow regions in and around underdense voids, marking the dynamical importance of voids in the local Universe. The maximum expansion rate of voids defines a sharp cut-off in the DTFE velocity divergence probability distribution function. We found that on the basis of this cut-off DTFE manages to consistently reproduce the value of $\Omega_{\rm m} \approx 0.35$ underlying the linearized velocity data set.

Key words: methods: numerical – methods: statistical – large-scale structure of Universe.

1 INTRODUCTION

The measurement and analysis of the peculiar velocities of galaxies forms a major probe of the cosmic structure formation process. The galaxy velocities reflect the large-scale matter flows which according to the gravitational instability scenario for cosmic structure formation go along with the formation and emergence of structure in the Universe. They are the response to the gradually unfolding underlying inhomogeneities in the cosmic matter distribution. As a result, the comparison of the induced cosmic flows on Mpc scales with the underlying matter distribution represents a potentially powerful instrument to further our insight into the dynamics of cosmic structure formation process and in inferring the values of a variety of key cosmological parameters.

Over the past two decades a major effort has been directed towards compiling large samples of galaxy peculiar velocities (see Dekel 1994; Strauss & Willick 1995, for reviews of the subject). By opening up the window on the dynamics of the cosmic structure formation process the analysis of these catalogues of galaxy peculiar velocities has led to enormous progress in our understanding of the process. This is particularly true for scales larger than $\gtrsim 10\,h^{-1}$ Mpc, scales on which structure formation still resides in the linear phase of development. In particular the Mark III catalogue, with an effective depth $\approx 60\,h^{-1}$ Mpc, stands as a landmark achievement (Willick et al. 1997).

★E-mail: emilio@pa.uky.edu (ER-D); weygaert@astro.rug.nl (RvdW)

Despite the successes progress has remained limited given the sizeable random and systematic errors that beset catalogues of peculiar velocities of galaxies and clusters. It allowed the mapping of the cosmic flow field in only a rather restricted volume of the nearby universe. Perhaps even more significant is that the low quality of the peculiar velocity data, in combination with their inhomogeneous and sparse spatial distribution, has prevented the development of an equally compelling and complete view of cosmic dynamics at the higher spatial resolution needed to probe and understand the dynamics of non-linear structures. It is on these scales of a few Mpc that the structure formation process has progressed to the more advanced quasi-linear stage and has left an imprint of genuinely recognizable cosmological structures and patterns. The characteristic flattened and filamentary features of the cosmic web, as well as the underdense void regions, are particularly outstanding examples. As yet it has not been possible to map the flows in and around these emerging structures.

Progress in the study of large-scale motions will not only depend on the availability of a substantially larger, better defined and considerably more accurate sample of galaxy peculiar velocities. Equally important will be the use of a more sophisticated machinery to handle the discrete, sparse and usually inhomogeneously sampled galaxy velocity data sets. It does remain a challenge to transform these into properly defined velocity maps throughout the surveyed volume. It brings to the fore the issues of interpolation of discrete data to any location within a given volume as well as the issue of the choice for a proper filtering prescription. As a consequence of the specific choices and assumptions involved with a particular method not all information inherent in the data set is preserved, and the resulting analysis does usually not include all available large- and small-scale properties of the peculiar velocity field. As for the first issue, the data interpolation, the measured peculiar velocities need to be interpolated into regions devoid of data. A conventional approach is that of interpolation of the discrete data set to regular grid locations by means of a fixed interpolation kernel. A notable example is that of the TSC kernel (see Hockney & Eastwood 1988). It is straightforward to show, however, that this will result in a mass-weighted quantity (Bernardeau & van de Weygaert 1996). This has confused comparisons with analytically derived results, as most of these concern volume-weighted quantities. The second aspect is that of the filter choice for the interpolation procedure. One may apply a *fixed*, *global* or *local* filter kernel. For sensibly defined field values it is important that data get filtered over an appropriately large volume. Amongst other, shot-noise effects should be suppressed. Conventionally, the galaxy peculiar velocities are filtered on a uniform fixed scale set by the requirement that also the sparsest sampled regions are properly averaged over. The resulting velocity map is one in which all the velocity information on scales smaller than the filter size has been filtered out. The most widely applied example is that of Gaussian filters (e.g. Bertschinger et al. 1990; Bernardeau et al. 1995; Fisher et al. 1995; Baker et al. 1998; Branchini et al. 1999; Dekel et al. 1999).

In this study we investigate the performance of the *Delaunay Tessellation Field Estimator* – DTFE – towards recovering the spatial density field and velocity flow in the nearby universe. DTFE is a self-adaptive density estimation and multidimensional interpolation scheme which does not make use of any artificial, user-specified filtering Schaap & van de Weygaert (2000). Currently DTFE is the most elaborate tessellation-based filter and interpolation scheme available to the field of astrophysics and astronomy (see Section 3.2). It belongs to a wider generic class of natural neighbour interpolations schemes. As a linear multidimensional field interpolation scheme DTFE may be regarded as the linear first-order equivalent of the higher order natural neighbour algorithms (NN-neighbour) for spatial interpolation (see Sibson 1981; Okabe et al. 2000).

DTFE and NN-neighbour schemes are based upon the use of the Voronoi and Delaunay tessellations of a given spatial discrete point set (Voronoi 1908; Delaunay 1934) (see Okabe et al. (2000) for an excellent and extensive overview). Voronoi and Delaunay tessellations epitomize a purely locally defined division of space. Their self-adaptive nature concerns both spatial resolution and local geometry, to which they adjust through their definition as region of influence amidst their *natural neighbours*. DTFE uses the high level of sensitivity of the Voronoi/Delaunay tessellation to the local point distribution to produce an estimate of the local density at each sample point (van de Weygaert 1991, 1994). For telling illustrations see Schaap & van de Weygaert (2007). Subsequently, it uses the Delaunay tessellation as multidimensional spatial interpolation grid. Unique within the context of NN-neighbour techniques, DTFE includes the explicit extension towards the self-adaptive determination of density fields on the basis of the spatial distribution of the point set itself, defined by Schaap & van de Weygaert (2000). Also important is that its linear nature ascertains its applicability to large data sets involving more than a million points.

We apply DTFE to the study of the spatial mass distribution and velocity field in the local Universe on the basis of a sample of galaxy positions and velocities inferred from the PSC*z* catalogue (Branchini et al. 1999). A uniform, densely sampled and fully volume-covering sample of galaxy peculiar velocities in the local Universe does not (yet) exist. We take the alternative of using the galaxy velocities and positions inferred from the uniform all-sky PSC*z* galaxy redshift sample. The PSC*z* galaxy sample is the last and best defined galaxy redshift selection from the *IRAS* catalogue (Saunders et al. 2000). This context guarantees the near uniform and well-defined depth and sky coverage essential for a self-consistent reconstruction of density and velocity fields within its volume of the nearby universe (Branchini et al. 1999; Schmoldt et al. 1999; Branchini et al. 2001; Teodoro et al. 2003). Although this involves a reconstruction on the basis of linear perturbation theory and the velocity field therefore does not contain proper non-linear components the spatial patterns outlined by the galaxies' positions do provide a reasonable spatial configuration to test DTFE over its ability to recover patterns in the velocity field.

This paper will demonstrate the virtues and potential of the DTFE method in the analysis of observational data, in particular in the capacity of DTFE to reveal intricate anisotropic patterns and that of rendering the multiscale character of both density and velocity fields. The objective of this study is first and foremost the production of maps of the volume-weighted velocity and density fields throughout the nearby universe. The self-adaptive nature of the DTFE technique yields an optimal resolution of the most interesting features, and this will enable the identification of characteristic patterns in the flow field and of their principal sources in the local density field. By default – to the DTFE method – this includes shear flows, (super)cluster infall and void outflow. By illuminating their relationship to the nearby and surrounding large-scale structures the DTFE procedure will help in increasing our understanding of the dynamics of the formation of the various structural components of the cosmic web (Bond, Kofman & Pogosyan 1996) (also see van de Weygaert 2002).

An additional aspect of the presented study is the DTFE performance in a non-uniformly sampled galaxy distribution. Because the PSC*z* galaxy catalogue on which our analysis is based involves a flux-limited selection of galaxies the sampling density

gradually decreases outward. While DTFE is capable of correcting the density values accordingly it also introduces a differential resolution scale along the reconstructed density and velocity field maps. While DTFE guarantees the preservation of an optimal share of information on the velocity field, this will automatically diminish with the outwardly decreasing selection function and the corresponding decrease in sampling density. The spectral coverage of the reconstructed DTFE fields will therefore be seriously affected towards the outer region of the PSCz volume, the velocity field reconstructions less so as they are dominated by lower frequency components.

We introduce the PSCz sample in Section 2, along with a short description of the linearization process to produce the sample of galaxy positions and (peculiar) velocities. This is followed by an outline of the DTFE procedure for density and velocity fields in Section 3. A cosmographic description of the spatial structures within the PSCz volume of the local Universe is contained in Section 4, after which in Section 5 we turn to the velocity flow field within the same volume. The issue of the differential spatial resolution of the DTFE density and velocity maps is discussed at some length in Section 6, while we describe some four specific features in the local Universe in Section 7. Finally, we discuss the spatial distribution of the velocity divergence field and its relation with the density distribution. Given the rather scant information on the velocity shear field we briefly treat its appearance in Section 9. Section 10 concludes our study with a summary and a description of prospects and relation to other work.

2 PSCz: GALAXY POSITIONS AND VELOCITIES

For the study of the structure and kinematics of the local cosmic neighbourhood we base ourselves upon the PSCz catalogue.

2.1 The PSCz sample

The *IRAS*-PSCz catalogue (Saunders et al. 2000) is an extension of the 1.2-Jy catalogue (Fisher et al. 1995). It contains ∼15 500 galaxies with a flux at 60 μm larger than 0.6 Jy. For a full description of the catalogue, selection criteria and the procedures used to avoid stellar contamination and galactic cirrus, we refer the reader to Saunders et al. (2000). For our purposes the most important characteristics of the catalogue are the large area sampled (∼84 per cent of the sky), its depth with a median redshift of 8500 km s^{-1}, and the dense sampling (the mean galaxy separation at 10 000 km s^{-1} is $\langle l \rangle = 1000\,\mathrm{km\,s^{-1}}$). It implies that PSC$z$ contains most of the gravitationally relevant mass concentrations in our local cosmic neighbourhood, certainly sufficient to explain and study the cosmic flows within a local volume of radius $\sim 120\,h^{-1}$ Mpc.

Because of the flux-limited nature of the PSCz catalogue, there is a decrease in the objects' sampling as a function of distance from the observer. This is quantified by the radial selection function of the catalogue, $\psi(r)$, where the selection function is defined as the fraction of the galaxy number density that is observed above the flux limit at some distance r. To ascertain the proper number density of objects each galaxy is weighed by the inverse of the selection function (see equation 2). For the selection function we used the expression $\psi(r)$ described in Branchini et al. (1999).

In addition to this selection function correction, further necessary corrections are that for the 16 per cent of the missing sky devoid of data, due to the cirrus emission and unobserved areas, and that for redshift distortions. Here we have followed Branchini et al. (1999) in using their spatially reconstructed PSCz catalogue.

2.2 PSCz: from redshift space to physical space

To translate the redshift-space distribution of galaxies in the PSCz catalogue into galaxy positions and velocities in real space we use base our study on a galaxy sample which has been processed by the linear theory for gravitational instability (Peebles 1980).

Our sample has been obtained along the lines of *method I* described in Branchini et al. (1999). The method is a specific realization of an iterative technique to minimize redshift-space distortions (Yahil et al. 1991). For a detailed exposition of the method we refer to Branchini et al. (1999). Starting with the original redshift distribution as input and computing the corresponding peculiar velocity fields, the spatial position of each galaxy is corrected accordingly. This is repeated in each iterative step until the spatial distribution of the galaxies and the inferred peculiar velocities are mutually consistent. In order to minimize the uncertainties derived from the lack of information on scales larger than the PSCz catalogue, the velocity predictions in the PSCz region were made in the Local Group frame.

In order to translate the distribution of galaxies into a gravitational field, and implied velocity field a value for the β parameter, the ratio between the linear velocity field factor $f(\Omega)$ (Peebles 1980) and the (supposedly) linear bias factor b between galaxy and mass density, needs to be assumed. A value of $\beta = 0.5$ has been adopted. The reliability of the corresponding modelled density and velocity has been confirmed in several studies, including density–density and velocity–velocity comparisons with other surveys (e.g. Branchini et al. 2001; Zaroubi et al. 2002). While the reconstruction procedure assumes linearity, one may expect its validity to extend into the early non-linear stages (Branchini et al. 1999). At hindsight, this claim may indeed be confirmed given the recovery by our DTFE technique of well-behaved mild non-linear density and velocity divergence distribution functions (see Fig. 6 and Section 9.4).

An important condition for a consistent linear reconstruction of the velocity and density field is that the density fluctuations should have a small amplitude. In order to ascertain this the gravity field has been smoothed with a top-hat filter whose radius is 500 km s^{-1} within the inner $50\,h^{-1}$ Mpc and subsequently increases following the average intergalaxy distance (see Fig. 2). An additional implicit requirement for the linearization process is that the vorticity modes in the peculiar velocity field are to be minimized. For the well-defined and representative sample of PSCz catalogue this is accomplished for $R \approx 5\,h^{-1}$ Mpc. For comparison, it may be worthwhile to realize that a Gaussian kernel of $12\,h^{-1}$ Mpc was employed by Dekel et al. (1999) to obtain a successful and representative linearization of the measured velocity field of the Mark III catalogue (Willick et al. 1997).

A complication for the linearization procedure is that of the velocity field around high-density regions. In the immediate surroundings of clusters of galaxies, the inflow of matter becomes so fast that they turn into triple-valued redshift regions. Romano-Díaz (2004) addressed this problem by considering two different samples. In one sample the triple-valued regions were collapsed, in the other they were not. Results showed that the implicit smoothing procedure of the linearization procedure minimizes this effect. Differences between collapsed and uncollapsed samples are less than 10 per cent for the bulk flow and velocity shear components, and consistent at the 1σ level. Here the velocity model which leaves the triple-valued regions uncollapsed has been followed.

The final product of the linearization velocity reconstruction procedure is a galaxy catalogue containing for each individual galaxy its *real spatial position* and its *peculiar velocity*. Our DTFE analysis

of the PSC*z* density and velocity fields is based upon this density and linearized velocity field.

3 THE DTFE METHOD

The DTFE interpolation method was introduced by Schaap & van de Weygaert (2000) (see also Schaap 2006), for rendering fully volume-covering and volume-weighted fields from a discrete set of sampled field values, including the density field as defined by the point sampling itself. DTFE involves an extension of the interpolation procedure described by Bernardeau & van de Weygaert (1996), who used Delaunay tessellations for the specific purpose of estimating the cosmic velocity divergence field, and showed the method's superior performance with respect to conventional interpolation procedures.

3.1 Voronoi and Delaunay tessellations

The DTFE method is based upon the *Voronoi and Delaunay tessellations* of the point sample (see Okabe et al. 2000, and references therein). A Delaunay tetrahedron is defined by the set of four points whose circumscribing sphere does not contain any of the other points in the generating set (Delaunay 1934) (triangles in two dimensions). The Delaunay tessellation is intimately related to the Voronoi tessellation of the point set, they are each others *dual*. The Voronoi tessellation of a point set is the division of space into mutually disjunct polyhedra, each polyhedron consisting of the part of space closer to the defining point than any of the other points (Voronoi 1908; Okabe et al. 2000). These spatial volume-covering divisions of space into mutually disjunct triangular (2D) or tetrahedral (3D) cells adapt to the local density and geometry of the point distribution.

Astronomical exploitation of Voronoi and Delaunay tessellations have as yet remained rather limited, despite the fact that a great many studies are based on observations which by their nature represent a discretely and irregularly sampled probe of an underlying smooth distribution. None the less, in recent years the self-adaptive virtues of Voronoi tessellations have been recognized in a gradually increasing stream of astronomical studies. Most of these seek to use the density sensitivity of Voronoi cell volumes and even Delaunay cell volumes to detect density peaks like clusters of galaxies amidst a general background of galaxies. In astronomy, the first application of Voronoi tessellations as density/intensity estimators was forwarded by Ebeling & Wiedenmann (1993), who sought to identify X-ray clusters as overdensities in X-ray photon counts. More recently, Ramella et al. (2001), Marinoni et al. (2002), Kim et al. (2002) and Lopes et al. (2004) used similar algorithms to isolate clusters within catalogues of galaxy positions produced by galaxy sky or redshift surveys. The explicit and additional ability of the more elaborate DTFE formalism to trace sharp density contrasts impelled Bradac et al. (2004) to compute the surface density map for a galaxy from the projection of the DTFE volume density field. The obtained surface density map was used to compute the gravitational lensing pattern around the object, upon which Li et al. (2006) evaluated the method in its ability to trace higher order singularities.

3.2 Local spatial adaptivity

The point in case for its pattern tracing characteristics is provided by the right-hand panel of Fig. 3 (also see fig. 4 in Schaap & van de Weygaert 2007), showing the 2D Delaunay triangulation for a section along the *Z*-supergalactic plane through the galaxy set which we analyse in this work, the PSC*z* catalogue. The DTFE method exploits these virtues and adapts automatically and in an entirely natural fashion to changes in the density or the geometry of the distribution of sampling points. Instead of involving user-defined filters which are based upon artificial smoothing kernels the resulting main virtue of DTFE is that it is intrinsically *self-adaptive*. In essence, it involves filtering kernels which are defined by the *local density and geometry* of the point process or object distribution. The Voronoi tessellation is used to obtain optimal *local* estimates of the spatial density (see section 8.5 Okabe et al. 2000), while the tetrahedra of its *dual* Delaunay tessellation are used as multidimensional intervals for linear interpolation of the field values sampled or estimated at the location of the sample points (Okabe et al. 2000, chapter 6).

On the basis of its interpolation characteristics DTFE is the first-order version of a wider class of tessellation-based *multidimensional* and entirely *local* interpolation procedures, commonly known as *natural neighbour interpolation* (Watson 1992; Sambridge, Braun & McQueen 1995; Sukumar 1998) (also see Okabe et al. 2000, chapter 6). In a variety of applied sciences the concept of natural neighbour interpolation and other advanced tessellation applications have already found wide application. Particularly successful and noteworthy examples may be found in computer visualization and surface rendering, geophysics (see e.g. Sambridge et al. 1995; Sambridge 1999) and engineering mechanics (Sukumar 1998).

3.3 DTFE: density and velocity fields

A crucial aspect of the success of the Delaunay interpolation procedure (Bernardeau & van de Weygaert 1996) is that it reproduces the *volume-weighted* velocity field, correcting a few fundamental biases in estimates of higher order velocity field moments. While, often unintentionally, most conventional interpolation schemes yield the *mass-weighted* velocity, it is the *volume-weighted* velocity estimate which figures in analytical expressions. This is particularly true for velocity field perturbation analyses within the context of gravitational instability scenarios based on primordial Gaussian perturbations. The validity of the Delaunay (and therefore also DTFE) velocity field interpolation scheme is perhaps most strongly emphasized by its success in reproducing the non-linear velocity divergence distribution function, specifically in its detailed agreement with second-order perturbation theory (Bernardeau & van de Weygaert 1996). The derived distribution function appears to be so accurate that it enables the accurate determination of cosmological parameters (Bernardeau & van de Weygaert 1997). This is even more interesting as a mild non-Gaussian velocity divergence distribution would enable the breaking of the degeneracy between the cosmic matter density Ω and the bias b between the matter and galaxy distribution (Bernardeau 1994; Łokas et al. 1995).

An essential and unique step of the DTFE procedure concerns the determination of field values at the sample points. For the velocity field this simply involves the measured velocities at the sample points. More complex is the issue for the density/intensity field. Tessellation-based methods for estimating the density have been introduced by Brown (1965) and Ord (1978). On the condition that the sample points are sampled proportionally to an underlying density/intensity field, the Voronoi tessellation is used to define optimal – local – density estimates (Okabe et al. 2000, section 8.5). A minor modification was introduced by Schaap & van de Weygaert (2000): in order to assure the mass-conserving nature of the DTFE interpolation procedure the sample point density estimates relate to the *contiguous* Voronoi cell (see Fig. 3).

Amongst the NN-neighbour schemes, DTFE is unique in including the tessellation-based density estimates on the basis of the

sampling point distribution itself. By restricting itself to a linear interpolation scheme it remains feasible to apply the method to data sets of millions of points. The latter is essential for the viability of the technique within a cosmological context.

3.4 DTFE and cosmic structure formation

Three major characteristics of the Mpc scale universe are the (1) the *web-like* spatial arrangement of galaxies and mass into elongated filaments, sheet-like walls and dense compact clusters, (2) the existence of large near-empty *void regions* and (3) the hierarchical nature of the mass distribution, marked by substructure over a wide range of scales and densities. According to the standard paradigm of cosmic structure formation, the theory of gravitational instability (Peebles 1980) this intricate spatial pattern has emerged as a result of the gravitational growth of tiny (Gaussian) density perturbations and the accompanying tiny velocity perturbations in the primordial Universe. Schaap & van de Weygaert (2007) demonstrate the ability of DTFE to successfully reproduce and quantify these key aspects of the non-linear web-like cosmic matter distribution in the Mpc universe.

(i) The hierarchically structured matter distribution is resolved to the smallest possible resolution scale set by the particle number density.

(ii) DTFE retains the morphology, i.e. shape of the features and patterns in the matter distribution. The characteristic anisotropic filamentary and planar features of the *cosmic web* are fully reproduced in the continuous DTFE density field.

(iii) The near-empty voids in the spatial matter distribution are reproduced optimally. Both their flat internal density distribution as well as their sharp outline and boundary are recovered in detail through the interpolation characteristics of the DTFE algorithm as well as by its tendency to suppress the shot-noise in these sparsely sampled regions (Schaap 2006).

The relation between the cosmic density and cosmic velocity field is an important piece of information on the dynamics of the cosmic structure formation process. When DTFE is applied to *N*-body simulations of structure formation, it does manage to successfully reproduce the physical and spatial correlation between cosmic density and velocity fields for highly non-linear structures. An early analysis of a GIF *N*-body simulation did show a few remarkable examples (see e.g. Schaap 2006): the velocity flows in and around the cores of high-density regions – for as long as it concerns single-stream laminar flows – are traced in detail by the DTFE density and velocity maps. Within the same simulations, the void-like regions were rendered as super-Hubble expanding bubbles, consistent with our view of void dynamics (Icke 1984; Sheth & van de Weygaert 2004). Considerably more detailed recent studies (Schaap & van de Weygaert 2003; Romano-Díaz 2004; Schaap 2006) confirmed that DTFE manages to trace the correspondence between velocity and density field over a large range of scales, resolving both small- and large-scale features of the velocity field.

Extrapolating this observation, and encouraged by the success of Voronoi-based methods in identifying dark haloes in *N*-body simulations (Neyrinck, Gnedin & Hamilton 2005) Arad, Dekel & Klypin (2004) used DTFE to assess the 6D phase-space density distribution of dark haloes in cosmological *N*-body simulations. While a fully 6D analysis may be computationally cumbersome (Ascasibar & Binney 2005), the splitting of the problem into a separate spatial and velocity-space 3D tessellation may indeed hold promise for an innovative analysis of the dynamical evolution of dark haloes.

3.5 DTFE: alternatives

The performance of DTFE has been tested extensively with respect to the performance of the rigid grid TSC method and the spatially adaptive smoothed particle hydrodynamics (SPH) method. The TSC procedure is rigid with respect to the spatial scale as well as the shape of the mass distribution. SPH kernels are adaptive with respect to the local density of points but lack sensitivity to the geometry of the mass distribution.

Schaap & van de Weygaert (2007) present numerous tests of the ability of DTFE to resolve spatial substructure and to detect anisotropic features. With respect to spatial resolution, DTFE manages not only to resolve maps of self-similar Soneira–Peebles models with the highest spatial resolution but also to recover the underlying scaling indices. Both the TSC and SPH fields fail completely in reproducing the proper scaling properties. While TSC does not produce any scaling at all, SPH does manage to reproduce scaling of the density field over a wide range of spatial scales. However, it fails fully in recovering the proper scaling indices. In addition, DTFE is also the only procedure whose density field has an *autocorrelation function* which agrees completely, down to the smallest scales, with the *two-point correlation function* of the Soneira–Peebles point distribution.

Also with respect to its ability to recover web-like features in the cosmic matter distribution the virtue of DTFE with respect to the TSC and SPH methods becomes more evident. While the SPH procedure fares considerably better than TSC its spherical smoothing kernel does introduce some artefacts and deficiencies when it gets to resolving the finest features. Defined by a fixed number of neighbours, SPH tends to smear out the smallest structures, particularly for anisotropically shaped ones, and results in features which occupy a significantly larger volume than the corresponding galaxy distribution. However, also DTFE patterns do contain some artefacts, of which the triangular imprint of its smoothing kernel is the most pronounced one.

3.6 The DTFE general reconstruction procedure

Fig. 1 describes the various stages of the DTFE field reconstruction procedure. It does so with reference to velocity field reconstruction. For a specification of the DTFE density field procedure we refer to Schaap (2006) (also see Schaap & van de Weygaert 2007). In summary, it consists of the following sequence of steps.

Point sample

Defining the spatial distribution of the point sample:

Density field

Point sample needs to be a general Poisson process of the (supposed) underlying density field, that is, it needs to be an unbiased sample of the underlying density field.

General (non-density) field

No stringent requirements upon the stochastic representativeness of the sampling process will be necessary except that the sample volume is adequately covered. In other words, the sample points need not form a uniform sample of the underlying density field.

Boundary Conditions

An important issue, with respect to the subsequent Delaunay tessellation computation and the self-consistency of the DTFE density and velocity field reconstructions, is that of the assumed boundary conditions. These will determine the Delaunay and Voronoi cells that overlap the boundary of the sample volume. Depending upon the sample at hand, a variety of options exists:

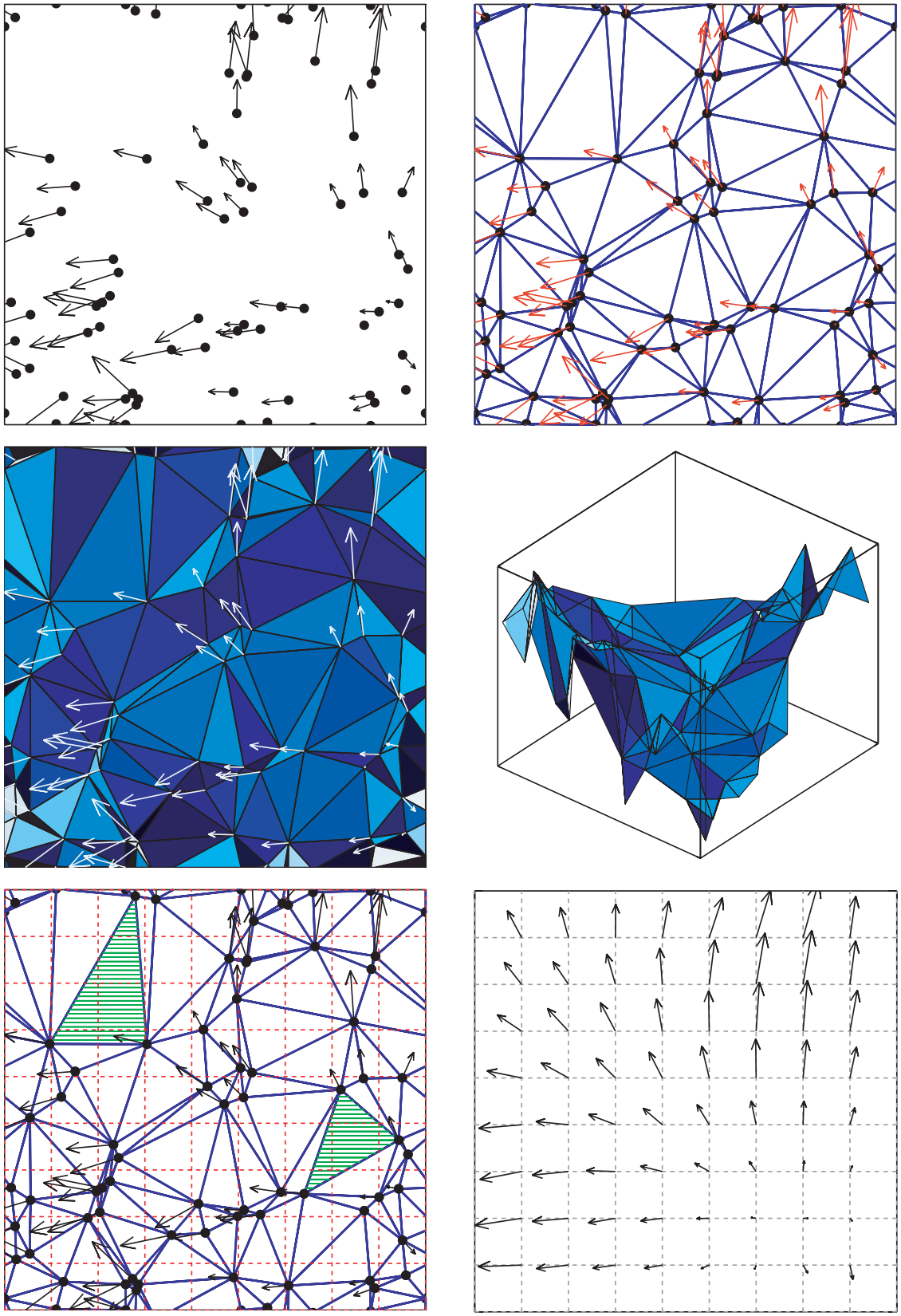

Figure 1. DTFE velocity interpolation procedure. The top right-hand panel presents the Delaunay triangulation of the discrete particle positions of the velocity field presented at the top left-hand panel. The central panels show the velocity gradient computed for each triangle. The colour scale corresponds to the amplitude of the determinant of the velocity gradient tensor. The right-hand panel depicts the 3D representation of the gradient surface. The height of each point corresponds to its velocity amplitude. The DTFE velocity field is estimated at the grid points indicated by the coloured grid of the bottom left-hand panel by assuming a linear variation of the velocity field. The bottom right-hand panel presents the outcome of the DTFE velocity interpolation procedure.

Vacuum boundary conditions
Outside the sample volume there are no points. This will lead to infinitely extended (contiguous) Voronoi cells surrounding sample points near the boundary. Evidently, these cells cannot be used for DTFE density field estimates and field interpolations: the volume of the DTFE reconstruction is smaller than that of the sample volume.

Periodic boundary conditions
The point sample is supposed to be repeated periodically in boundary boxes, defining a toroidal topology for the sample volume. The resulting Delaunay and Voronoi tessellations are also periodic, their total volume exactly equal to the sample volume. While specific periodic tessellation algorithms do exist (van de Weygaert 1994), this is not yet true for most available routines in standard libraries. For the analysis of *N*-body simulations this is the most straightforward and preferable choice.

Buffer conditions
The sample volume box is surrounded by a buffer zone filled with a synthetic point sample. The density of the synthetic buffer point sample should be related to the density in the nearby sample volume. The depth of the buffer zone depends on the density of the synthetic point sample, it should be sufficiently wide for any Delaunay or Voronoi cell related to a sample point not to exceed the buffer zone. A clear condition for a sufficiently deep buffer zone has been specified by Neyrinck et al. (2005). When involving velocity field analysis, the velocities of the buffer points should also follow the velocity distribution of the sample and be in accordance with the continuity equation. Relevant examples of possible choices are:

– *internal*: the analysed sample is a subsample embedded within a large sample volume, a sufficient number of these sample points outside the analysis volume is taken along in the DTFE reconstruction.

– *random cloning technique*: akin to the technique described by Yahil et al. (1991).

– *constrained random field*: realizations employing the existing correlations in the field (Bertschinger 1987; Hoffman & Ribak 1991; van de Weygaert & Bertschinger 1996).

Delaunay tessellation
Construction of the Delaunay tessellation from the point sample (see Fig. 3). While we still use our own Voronoi-Delaunay code van de Weygaert (1994), at present there is a score of efficient library routines available. Particularly noteworthy is the CGAL initiative, a large library of computational geometry routines[1]

Field values point sample
Dependent on whether it concerns the densities at the sample points or a measured field value there are two options:

General (non-density) field
(Sampled) value of field at sample point.

Density field
The density values at the sampled points are determined from the corresponding Voronoi tessellations. The estimate of the density at each sample point is the normalized inverse of the volume of its *contiguous* Voronoi cell $\mathcal{W}_i$ of each point i. The *contiguous Voronoi cell* of a point i is the union of all Delaunay tetrahedra of which point i forms one of the four vertices (see Fig. 3, second frame, for an illustration). We recognize two applicable situations:

– *Uniform sampling process*: the point sample is an unbiased sample of the underlying density field. Typical example is that of *N*-body simulation particles. For *D*-dimensional space the density estimate is,

$$\widehat{\rho}(\boldsymbol{x}_i) \,=\, (1+D)\,\frac{w_i}{V(\mathcal{W}_i)}, \tag{1}$$

with w_i the weight of sample point i, usually we assume the same 'mass' for each point.

– *Systematic non-uniform sampling process*: sampling density according to specified selection process. The non-uniform sampling process is quantified by an a priori known selection function $\psi(\boldsymbol{x})$. This situation is typical for galaxy surveys, $\psi(\boldsymbol{x})$ may encapsulate differences in sampling density $\psi(\alpha, \delta)$ as function of sky position (α, δ), as well as the radial redshift selection function $\psi(r)$ for magnitude- or flux-limited surveys. For *D*-dimensional space the density estimate is

$$\widehat{\rho}(\boldsymbol{x}_i) \,=\, (1+D)\,\frac{w_i}{\psi(\boldsymbol{x}_i)\,V(\mathcal{W}_i)}. \tag{2}$$

Field Gradient
Calculation of the field gradient estimate $\widehat{\nabla f}|_m$ in each *D*-dimensional Delaunay simplex m ($D = 3$: tetrahedron; $D = 2$: triangle) by solving the set of linear equations for the field values at the positions of the $(D + 1)$ tetrahedron vertices,

$$\widehat{\nabla f}|_m \Longleftarrow \begin{cases} f_0 & f_1 & f_2 & f_3 \\ \boldsymbol{r}_0 & \boldsymbol{r}_1 & \boldsymbol{r}_2 & \boldsymbol{r}_3 \end{cases} \tag{3}$$

Evidently, linear interpolation for a field f is only meaningful when the field does not fluctuate strongly. Particularly relevant for velocity field reconstructions is that there should be no orbit crossing flows within the volume of the Delaunay cell which would involve multiple velocity values at any one location. In other words, DTFE velocity field analysis is only significant for *laminar* flows.

Note that in the case of the sampled field being the velocity field $\boldsymbol{v}$ we may not only infer the velocity gradient in a Delaunay tetrahedron, but also the directly related quantities such as the *velocity divergence*, *shear* and *vorticity*.

Interpolation
The final basic step of the DTFE procedure is the field interpolation. The processing and post-processing steps involve numerous interpolation calculations, for each of the involved locations $\boldsymbol{x}$. Given a location $\boldsymbol{x}$, the Delaunay tetrahedron m in which it is embedded is determined. On the basis of the field gradient $\widehat{\nabla f}|_m$ the field value is computed by (linear) interpolation,

$$\widehat{f}(\boldsymbol{x}) \,=\, \widehat{f}(\boldsymbol{x}_i) \,+\, \widehat{\nabla f}\Big|_m \cdot (\boldsymbol{x} - \boldsymbol{x}_i). \tag{4}$$

In principle, higher order interpolation procedures are also possible. Two relevant procedures are:
– spline interpolation
– natural neighbour interpolation.
Implementation of natural neighbour interpolations is presently in progress.

Processing
Though basically of the same character for practical purposes we make a distinction between straightforward processing steps concerning the production of images and simple smoothing filtering operations on one hand, and more complex post-processing on the other hand. The latter are treated in the next item. Basic to the

[1] CGAL is a c^{++} library of algorithms and data structures for computational geometry, see www.cgal.org.

processing steps is the determination of field values following the interpolation procedure(s) outlined above.
Straightforward 'first line' field operations are *'image reconstruction'* and, subsequently, *'smoothing/filtering'*.

Image reconstruction
For a set of *image points*, usually grid points, determine the *image value*: formally the average field value within the corresponding grid cell. In practice a few different strategies may be followed, dictated by accuracy requirements. These are:

– *Formal geometric approach*
Integrate over the field values within each grid cell. This implies the calculation of the intersection of the relevant Delaunay tetrahedra and integration of the (linearly) running field values within the intersection. Subsequently the integrands of each Delaunay intersection are added and averaged over the grid-cell volume.

– *Monte Carlo approach*
Approximate the integral by taking the average over a number of (interpolated) field values probed at randomly distributed locations within the grid cell around an *image point*. Finally, average over the obtained field values within a grid cell.

– *Singular interpolation approach*
A reasonable and usually satisfactory alternative to the formal geometric or Monte Carlo approach is the shortcut to limit the field value calculation to that at the (grid) location of the *image point*. This offers a reasonable approximation for grid cells which are smaller or comparable to that of intersecting Delaunay cells, on the condition the field gradient within the cell(s) is not too large.

Smoothing and filtering
Linear filtering of the field $\widehat{f}$: Convolution of the field $\widehat{f}$ with a filter function $W_s(\boldsymbol{x}, \boldsymbol{y})$, usually user specified,

$$f_s(\boldsymbol{x}) = \int \widehat{f}(\boldsymbol{x}')\, W_s(\boldsymbol{x}', \boldsymbol{y})\, \mathrm{d}\boldsymbol{x}'. \quad (5)$$

Post-processing
The real potential of DTFE fields may be found in sophisticated applications, tuned towards uncovering characteristics of the reconstructed fields. An important aspect of this involves the analysis of structures in the density field. Some notable examples are:

– Advanced filtering operations. Potentially interesting applications are those based on the use of wavelets (Martínez et al. 2005).

– Cluster, filament and wall detection by means of the *multiscale morphology filter* (Aragon et al. 2007).

– Void identification on the basis of the *cosmic watershed* algorithm (Platen, van de Weygaert & Jones 2007).

– Halo detection in *N*-body simulations (Neyrinck et al. 2005).

– The computation of 2D surface densities for the study of gravitational lensing (Bradac et al. 2004).

In addition, DTFE enables the simultaneous and combined analysis of density fields and other relevant physical fields. As it allows the simultaneous determination of *density* and *velocity* fields, it can serve as the basis for studies of the dynamics of structure formation in the cosmos. Its ability to detect substructure as well as reproduce the morphology of cosmic features and objects implies DTFE to be suited for assessing their dynamics without having to invoke artificial filters.

– DTFE as basis for the study of the full *phase-space* structure of structures and objects. The phase-space structure dark haloes in cosmological structure formation scenarios has been studied by Arad et al. (2004).

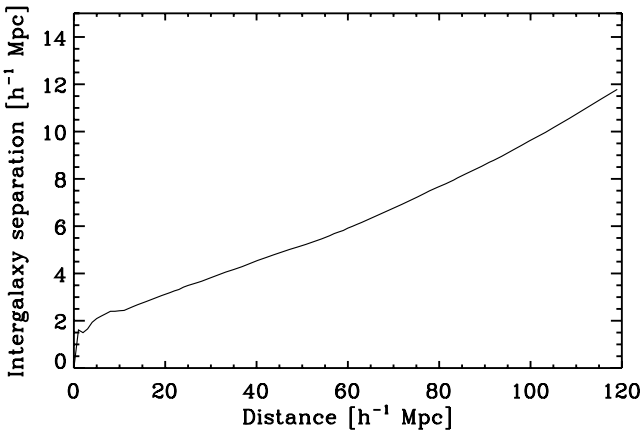

Figure 2. The (mean) PSC*z* intergalaxy distance as a function of distance (to the Local Group), an expression of the diminishing sampling density in the flux-limited PSC*z* sample.

4 PSC*z*: TOWARDS THE DTFE DENSITY AND VELOCITY FIELDS

Given the determination of the *positions* and *velocities* of the PSC*z* galaxies in our sample by the linearization procedure of Branchini et al. (1999), the continuous volume-weighted DTFE density and velocity fields – and the corresponding velocity divergence and shear field – throughout the sample volume is computed following the steps outlined in Section 3.6.

In our study we analyse and assess the DTFE density and velocity maps within an inner region of radius $120\,h^{-1}$ Mpc. It allows a more than qualitative comparison with the analysis of Branchini et al. (1999) and Schmoldt et al. (1999). Out to this radius the sample contains 10 651 galaxies. To include a sufficiently large region enclosing the main sources gravitationally contributing to the velocity field in the inner $120\,h^{-1}$ Mpc we make use of the data within a spherical volume of radius $180\,h^{-1}$ Mpc (Branchini et al. 1999; Romano-Díaz 2004). Out to this radius the PSC*z* sample still has sufficient structure resolution, without shot-noise becoming dominant. The number of galaxies in this 'PSC*z*-source' sample out to this radius is 13 432.

An important factor to take into account in the interpretation and analysis of the resulting DTFE field maps is the fact that the intergalaxy separation is an increasing function of distance. For the PSC*z* sample it rises from near $\approx 2\,h^{-1}$ Mpc within a radius from 20 to $\approx 14\,h^{-1}$ Mpc at the outer radius of $120\,h^{-1}$ Mpc (see Fig. 2). As a result the Delaunay tessellation polyhedra will gradually grow in volume as a function of distance. Because it are the polyhedral cells which set the local resolution of the interpolated fields we need to take into account that the pure DTFE reconstruction maps have a diminishing resolution towards larger distances. This makes post-processing a necessity step for a quantitative analysis and/or for an objective assessment of the resulting density and velocity fields.

4.1 PSC*z*: the Delaunay map

The spatial positions and peculiar velocities of the galaxies in the processed PSC*z* sample are depicted in the left-hand panel of Fig. 3. The figure shows the galaxies within a slice of $2.5\,h^{-1}$ Mpc thickness centred along the *Z*-supergalactic plane. The Local Group is located

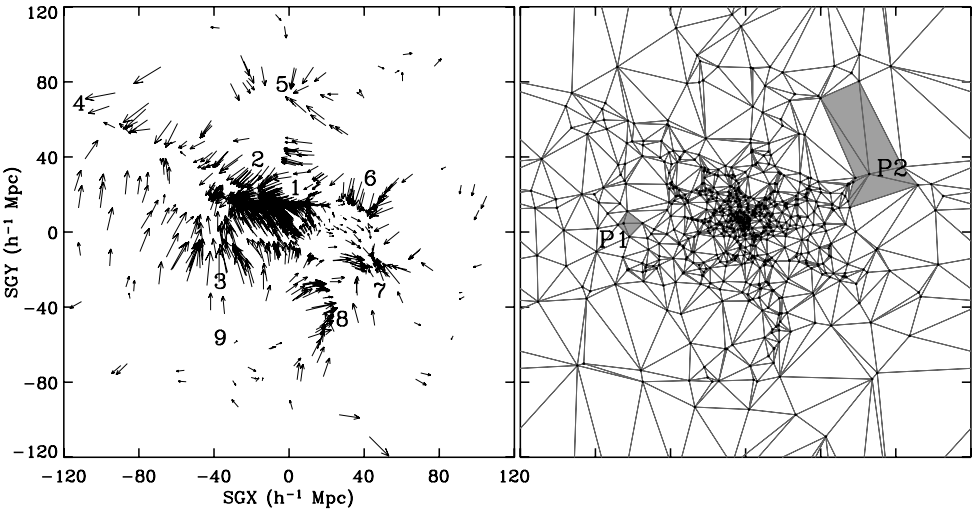

Figure 3. Modelled peculiar velocity field at the galaxy positions (left-hand panel). The plot represents a slice of $2.5\,h^{-1}$ Mpc thickness centred along the *Z*-supergalactic plane. Numbers indicate the major visible structures along the section. 1 – Local Supercluster, 2 – GA region, 3 – Pavo–Indus–Telescopium complex, 4 – Shapley supercluster, 5 – Coma cluster, 6 – Camelopardalis cluster, 7 – Pisces–Perseus supercluster, 8 – Cetus wall, 9 – Sculptor void. (From Branchini et al. 1999). The right-hand panel shows the corresponding Delaunay tessellation of the galaxy distribution. The shadowed regions illustrate the 'contiguous Voronoi cell' concept for two galaxies, marked P1 and P2.

at the origin. Velocity vectors, indicating the velocity component within the supergalactic plane, are plotted at the galaxy positions. The size of the velocity vectors is normalized with respect to the maximum velocity amplitude within the slice. In the map the main large-scale structures have been labelled. For a description of these we refer to Section 5.1.

For reference the right-hand frame depicts the Delaunay triangulation defined by the projected positions of the sample galaxies within the $2.5\,h^{-1}$ Mpc thick slice around supergalactic plane. By showing the meticulous spatial adaptivity of the Delaunay tessellation, it forms a good illustration of the rationale behind using it as an estimate for local density. The figure emphasizes this by means of the two grey areas, the *contiguous Voronoi cells* surrounding a sample point. The inverse of these form the DTFE method's local density estimate (see equation 1). The figure also provides a good impression of the corresponding non-uniform spatial resolution of the Delaunay interpolation grid. The spatial resolution of the DTFE interpolation grid follows the density of the sample points.

4.2 PSC*z*: the DTFE interpolation

Once the spatial position $\boldsymbol{r}_n$ and velocity $\boldsymbol{v}_n$ of each galaxy n in our PSC*z* sample has been determined, DTFE will be applied towards reconstructing density and velocity fields throughout the sample volume.

4.2.1 PSCz DTFE density values

Evidently, the calculation of the Delaunay tessellation needs to be done only once, for both the density and velocity fields. While the velocity values $\boldsymbol{v}_n$ at the locations $\boldsymbol{r}_n$ are part of the input information, the density values are estimated from the volume $V(\mathcal{W})_n$ of the surrounding *contiguous Voronoi cell* $\mathcal{W}_n$ around each cell n (see Fig. 3). For the 3D density maps of the magnitude-limited PSC*z* survey we have the density estimates (Schaap & van de Weygaert 2000)

$$\widehat{\rho}(\boldsymbol{x}_n) = \frac{4}{\psi_{\mathrm{PSC}z}(\boldsymbol{x}_n)\, V(\mathcal{W}_n)}. \tag{6}$$

For the PSC*z* radial selection function $\psi_{\mathrm{PSC}z}$ we used the expression described in Branchini et al. (1999).

4.2.2 DTFE density and velocity gradients

The value of the density and velocity field gradient in each Delaunay tetrahedron is directly and uniquely determined from the location $\boldsymbol{r} = (x, y, z)$ of the four points forming the Delaunay tetrahedron's vertices, $\boldsymbol{r}_0$, $\boldsymbol{r}_1$, $\boldsymbol{r}_2$ and $\boldsymbol{r}_3$, and the value of the estimated density and sampled velocities at each of these locations, $(\widehat{\rho}_0, \boldsymbol{v}_0)$, $(\widehat{\rho}_1, \boldsymbol{v}_1)$, $(\widehat{\rho}_2, \boldsymbol{v}_2)$ and $(\widehat{\rho}_3, \boldsymbol{v}_3)$,

$$\begin{pmatrix} \widehat{\nabla\rho|_m} \\ \widehat{\nabla\boldsymbol{v}|_m} \end{pmatrix} \Longleftarrow \begin{cases} \widehat{\rho}_0 & \widehat{\rho}_1 & \widehat{\rho}_2 & \widehat{\rho}_3 \\ \boldsymbol{v}_0 & \boldsymbol{v}_1 & \boldsymbol{v}_2 & \boldsymbol{v}_3 \\ \boldsymbol{r}_0 & \boldsymbol{r}_1 & \boldsymbol{r}_2 & \boldsymbol{r}_3 \end{cases} \tag{7}$$

The four vertices of the Delaunay tetrahedron are both necessary and sufficient for computing the entire 3×3 velocity gradient tensor $\partial v_i/\partial x_j$. Evidently, the same holds for the density gradient $\partial\rho/\partial x_j$. We define the matrix $\mathbf{A}$ is defined on the basis of the vertex distances $(\Delta x_n, \Delta y_n, \Delta z_n)$ (n = 1,2,3),

$$\begin{pmatrix} \Delta x_n = x_n - x_0 \\ \Delta y_n = y_n - y_0 \\ \Delta z_n = z_n - z_0 \end{pmatrix} \quad \Longrightarrow \quad \mathbf{A} = \begin{pmatrix} \Delta x_1 & \Delta y_1 & \Delta z_1 \\ \Delta x_2 & \Delta y_2 & \Delta z_2 \\ \Delta x_3 & \Delta y_3 & \Delta z_3 \end{pmatrix}. \tag{8}$$

Similarly defining $\Delta\boldsymbol{v}_n \equiv \boldsymbol{v}_n - \boldsymbol{v}_0 (n = 1, 2, 3)$ and $\Delta\ \rho_n \equiv \rho_n - \rho_0$ $(n = 1, 2, 3)$ it is straightforward to compute directly and simultaneously the density field gradient $\nabla\ \rho|_m$ and the velocity field gradient

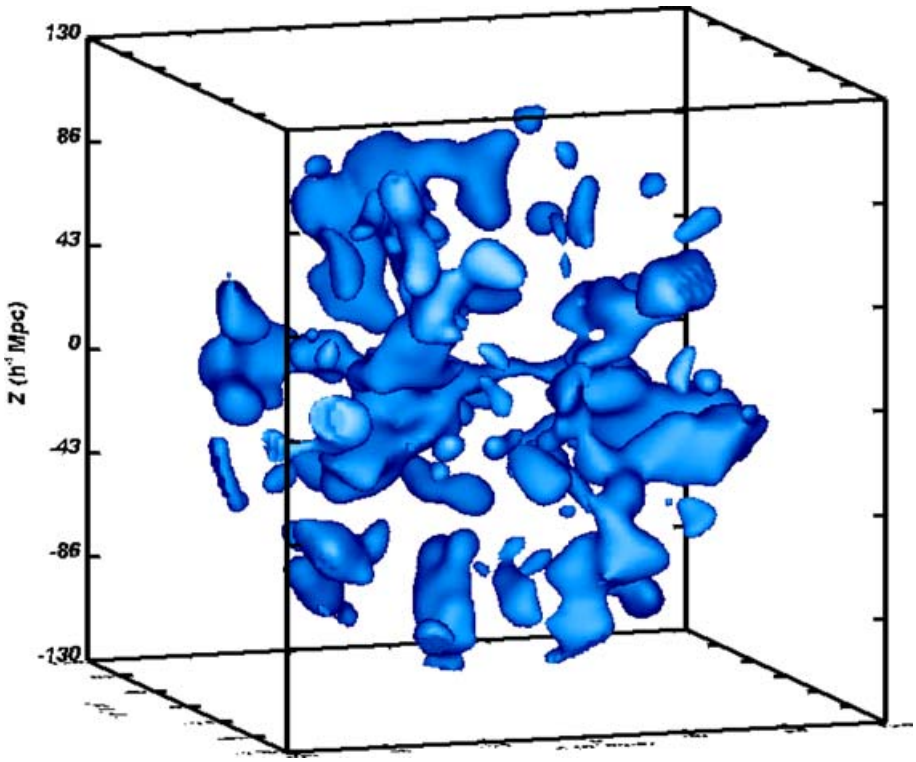

Figure 4. 3D reconstructed DTFE PSCz density field. The field has been smoothed with a Gaussian kernel of $5\,h^{-1}$ Mpc (for the effective smoothing scale see text, Section 4.2.3). The isosurface represents structures at three times the smoothed the mean density. Note the two huge density concentrations around the $Z = 0$ plane, the Pisces–Perseus and Cetus wall complex to the right-hand side, and the Hydra–Centaurus and Pavo–Indus–Telescopium to the left-hand side. A well-delineated bridge connects both structures, the Local Supercluster. For feature identity see the numbers in Fig. 3.

$\nabla \boldsymbol{v}\,|_m = \partial\, v_i/\partial\, x_j$ in Delaunay tetrahedron m via the inversion

$$\begin{pmatrix} \frac{\partial \rho}{\partial x} \\ \frac{\partial \rho}{\partial y} \\ \frac{\partial \rho}{\partial z} \end{pmatrix} = \mathbf{A}^{-1} \begin{pmatrix} \Delta\rho_1 \\ \Delta\rho_2 \\ \Delta\rho_3 \end{pmatrix} ;$$

$$\begin{pmatrix} \frac{\partial v_x}{\partial x} & \frac{\partial v_y}{\partial x} & \frac{\partial v_z}{\partial x} \\ \frac{\partial v_x}{\partial y} & \frac{\partial v_y}{\partial y} & \frac{\partial v_z}{\partial y} \\ \frac{\partial v_x}{\partial z} & \frac{\partial v_y}{\partial z} & \frac{\partial v_z}{\partial z} \end{pmatrix} = \mathbf{A}^{-1} \begin{pmatrix} \Delta v_{1x} & \Delta v_{1y} & \Delta v_{1z} \\ \Delta v_{2x} & \Delta v_{2y} & \Delta v_{2z} \\ \Delta v_{3x} & \Delta v_{3y} & \Delta v_{3z} \end{pmatrix} . \quad (9)$$

4.2.3 DTFE: velocity field constraints

DTFE interpolation of velocity field values is only feasible in regions devoid of multistream flows. As soon as there are multiple flows – notably in high-density cluster concentrations or in the highest density realms of the filamentary and planar caustics in the cosmic web – the method breaks down and cannot be applied.

In the study presented here this is particularly so in high-density clusters. The complication can be circumvented by filtering the velocities over a sufficiently large region, imposing an additional resolution constraint on the DTFE velocity field. Implicitly this has actually already been accomplished in the linearization procedure of the velocity fields preceding the DTFE processing (see Section 2). The linearization of the input velocities involves a kernel size of $\sqrt{5}\,h^{-1}$ Mpc[2] for the inner $50\,h^{-1}$ Mpc, for larger distances it gradually increases with the intergalaxy distance $l(r)$ as $l(r)/\sqrt{5}\,h^{-1}$ Mpc (for the PSCz intergalaxy distance see Fig. 2). As a result, the resolution of the velocity field is set to a lower limit of $\sqrt{5}\,h^{-1}$ Mpc. This is sufficient to assure the viability of the DTFE velocity field reconstructions.

5 PSCz: THE DTFE DENSITY FIELD

To appreciate the power of the DTFE method, the 3D map of the DTFE density field in Fig. 4 provides a telling illustration. For consistency between density field and the velocity field, the density field has been smoothed with a Gaussian kernel of $\sqrt{5}\,h^{-1}$ Mpc. Note that for $r \gtrsim 50\,h^{-1}$ Mpc the resolution of both density and velocity fields increases proportional to the intergalaxy distance $l(r)$: while the velocity field linearization procedure of Branchini et al. (1999) explicitly involves this as effective smoothing radius the DTFE adaptive grid resolution automatically scales accordingly (see Section 7.1). The depicted isosurface level corresponds to structures at three times the smoothed mean density. On these scales most outstanding features correspond to supercluster or void regions of the cosmic web.[3]

Many familiar features are concentrated near the Z-supergalactic plane of the 3D density field. For identification of the various

[2] We have used the fact that $R_{\rm G} = R_{\rm TH}/\sqrt{5}$ (Suto & Fujita 1990).

[3] Note that here, and throughout this study, the density field δ is in effect the galaxy density field $\delta_{\rm g}$. It may be a biased reflection of the true matter density field δ_m, here parametrized by a linear bias factor b.

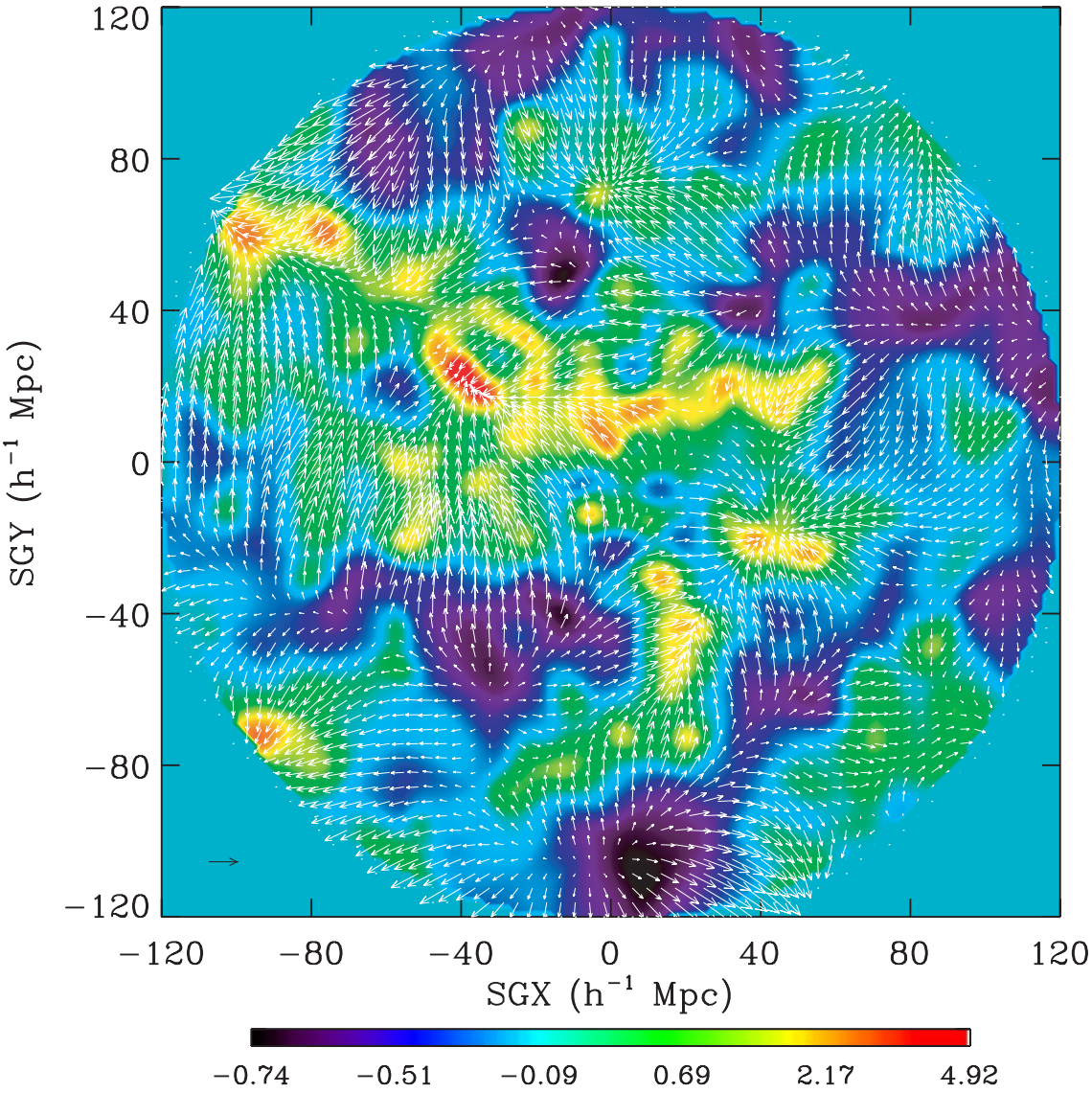

Figure 5. DTFE density and velocity fields projected along the *Z*-supergalactic plane in a thin slice. The colour bar indicates the plotted density scale. The density and velocity fields have an effective Gaussian smoothing radius of $R_G \sim \max \sqrt{5}, l(r)\sqrt{5}\, h^{-1}$ Mpc, with $l(r)$ the intergalaxy separation distance. Density values are scaled according to the bar at the bottom of the frame, while the velocity vectors are scaled such that the (black) velocity vector at the bottom left-hand side corresponds to 650 km s^{-1}.

features we show the density field in this plane by means of the contour colour map in Fig. 5. The amplitude of the corresponding density values can be inferred from the colour bar below the map. The superimposed arrows indicate the corresponding DTFE reconstructed velocities within the supergalactic plane (see Section 6).

It is interesting to compare the density map in Fig. 5 with the map in fig. 5 of Branchini et al. (1999). This also involves a density field, of the same PSC*z* volume, smoothed with a Gaussian filter with a smoothing scale which spatially adapts itself to the local (galaxy) density. While it shares the superb spatial resolution with the DTFE map, the imprint of the underlying (spherical) Gaussian filter is particularly visible in the boundary regions of voids and superclusters. The work by Schaap & van de Weygaert (2007) shows that its lack of geometric adaptivtiy causes structural artefacts near boundaries of low-density voids and anisotropic filaments.

5.1 The DTFE density field: cosmography

The Local Group is located at the origin of the maps in Figs 3 and 4 and in Fig. 5, it is embedded in the surrounding Local Supercluster region. On the basis of their gravitational influence on the surroundings, manifest in the corresponding velocity field, most of the main large-scale structures can be easily recognized in Fig. 3. For the purpose of guidance and identification we have inserted labels in the map of the supergalactic plane galaxy positions in Fig. 3, indicating the various large-scale structures in our neighbourhood.

High-density regions (reddish regions) as well as low-density ones (dark zones) can be easily recognized along the isodensity map in Fig. 4. One of the immediate observations is that the high-density regions, particularly the highly resolved one in the inner region of the 3D map, tend to be flattened or elongated, a direct consequence

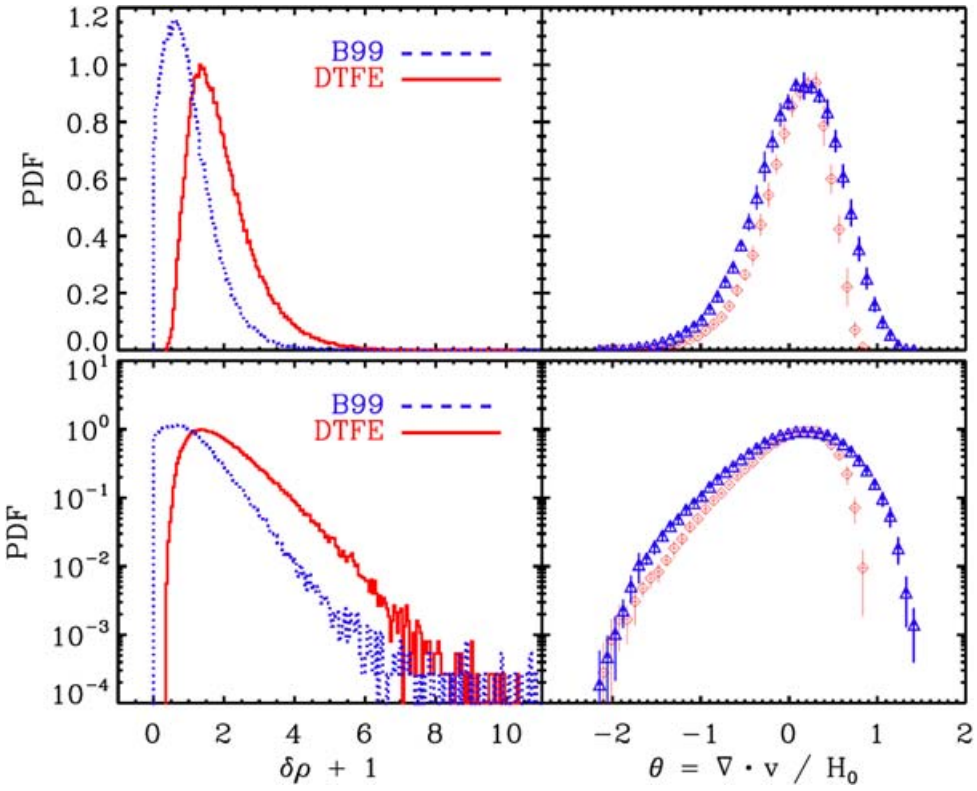

Figure 6. Density and velocity PDFs for PSC*z*. In the top row the PDFs are plotted in lin–lin, in the bottom row in lin–log. The lin–lin plots emphasize the level of non-Gaussianity of the density and velocity fields. The lin–log plot emphasizes prominent features in the distribution, in particular the sharply defined low-density edge, and facilitates comparison between the velocity divergence PDF and the density PDF. Left-hand panels: PDF of the DTFE density field (solid line). For comparison we have included the density PDF from of Branchini et al. (2002, dashed line). Right-hand panels: the PDF of the velocity divergence (see Section 9). The DTFE velocity divergence distribution is indicated by means of diamonds, the Branchini et al. (1999) one as triangles (only in the lin–log plot) as triangles. Note the good mirror image correspondence between the density and velocity divergence plot for the DTFE fields (both lin–lin and lin–log).

of the DTFE ability to trace and reproduce the natural shape and anisotropy of structural features.

Two major matter concentrations along the $Z = 0$ plane dominate the field (Fig. 5). The complex formed by the Pavo–Indus–Telescopium supercluster and the Hydra–Centaurus supercluster with its extension towards the Shapley concentration dominates the left-hand region of the supergalactic plane (the orientation of the figure is such that the Pavo–Indus–Telescopium supercluster, at [SGX, SGY] $\approx [-40, -10]\,h^{-1}$ Mpc, is visible at the front left-hand side in the 3D image). Towards the other direction of the Local Supercluster we find a similar outstanding mass concentration. Centrally located is the Pisces–Perseus supercluster, extending out in the Cetus wall to the south and the Camelopardalis cluster towards the north. The Pisces–Perseus supercluster, clearly visible at [SGX, SGY] $\approx [45, -20]\,h^{-1}$ Mpc, and the Cetus wall, at [SGX, SGY] $\approx [20, -40]\,h^{-1}$ Mpc and connecting with the barely visible Sculptor wall at [SGX, SGY] $\approx [0, -80]\,h^{-1}$ Mpc, overshadow the other structures. The massive matter concentrations on either side of the Local Supercluster are connected by a thin filamentary bridge, passing near the origin of the map and outlining the Local Supercluster. The filament runs from the Camelopardalis cluster ([SGX, SGY] $\approx [45, 20]\,h^{-1}$ Mpc) towards the Shapley supercluster ([SGX, SGY] $\approx [-120, 70]\,h^{-1}$ Mpc) and connects the Local Supercluster with the Hydra–Centaurus supercluster.

The Hydra–Centaurus supercluster, connecting with the Local Supercluster on the north-west side, may be largely identified with the Great Attractor (GA) region. Also the Shapley concentration, further out along the north-west axis, may be a major contributor to the velocity flows in the Local Supercluster. This can be inferred from Fig. 3, which shows that the modelled linearized velocity field does not show any evidence for a backflow into the GA region (e.g. Basilakos & Plionis 1998; Plionis & Kolokotronis 1998; Branchini et al. 1999; Rowan-Robinson et al. 2000). It might be the result of a mere artefact of the reconstruction procedure while it did reveal itself in the map computed by means of the alternative procedure of Schmoldt et al. (1999). Recent studies of the dipole in the X-ray cluster distribution (Kocevski & Ebeling 2006) do indeed provide ample influence for a major dynamical influence of the Shapley concentration, be it that the more localized Two Micron All Sky Survey sample appears to suggest that the tug of the GA remains the overriding influence for the Local Supercluster (Erdoğdu et al 2006).

The GA complex and its extension towards the Shapley configuration, the Local Supercluster and the Pisces–Perseus complex do define a dynamical axis of a suggestive quadrupolar configuration. The *tug of war* between the GA and the Pisces–Perseus will be expressed in terms of a strong compressional tidal force perpendicular to the axis, responsible for the filamentary geometry and the strong velocity shear near the Local Supercluster (Lilje, Yahil & Jones 1986), (also see van de Weygaert & Bertschinger 1996). In all, the map of Fig. 4 forms a wonderful illustration of the theoretical framework of the cosmic web by Bond et al. (1996), in which the large-scale tidal field is the web-shaping agent.

Perpendicular to the dynamical axis defined by the GA complex, Local Supercluster and the Pisces–Perseus complex, the most outstanding feature in our local cosmic neighbourhood is the Coma

cluster. It is visible as the only major concentration at the top of the map, at [SGX, SGY] $\approx [0, 70]\,h^{-1}$ Mpc, embedded within the Coma wall of which the maps also allow a glimpse.

Also highly interesting are the voids visible in the DTFE density map in the local Universe. These can be readily identified from the 3D map of Fig. 4 – and even better from its underdense mirror image – as large empty (and in general roundish) regions. The Sculptor void, surrounded by the Pavo–Indus–Telescopium complex and the Sculptor and Cetus walls, is one of the most salient empty features along the supergalactic plane. Its impact on the surrounding velocity field can be easily recognized (see Fig. 3). The Fornax void is located just at the bottom of the plot ([SGX, SGY] $\approx [10, -110]\,h^{-1}$ Mpc). Also the small void located between the Coma cluster and the Hydra–Centaurus region is clearly delineated.

5.2 The DTFE density field: probability distribution function

Its ability to resolve small- and large-scale structure without loss of spatial resolution and the ability to meaningfully interpolate the density field in poorly sampled void regions allows DTFE to recover the density probability distribution function (PDF), including both the low- and high-density ends of the PDF. Fig. 6 shows the resulting distribution function: the solid lines in the left-hand frames (top: lin–lin, bottom: lin–log) show the PDF of the DTFE density field. The intimate connection with the PDF of the corresponding velocity divergence distribution will be discussed in Section 9.4. By assessing the PDF of the density and flow field restricted to the inner $50\,h^{-1}$ Mpc of the PSCz volume and observing it to be largely in agreement with that for the full sample seen here we reassured ourselves that effects resulting from the heterogeneous spatial resolution (see Section 7.1) do not substantially affect our results.

On the positive side of the PDF DTFE manages to trace the distribution function down to PDF values of 10^{-3}, on the negative side down to even lower values. One direct observation is that the DTFE PDF does not go down to density values of -1. The lin–lin plot in the left-hand frame nicely shows the mild non-Gaussian character of the density field, entirely according to expectation. The lin–log plot emphasizes the meticulous rendering of the low-density regions: on the low-density side there is a sharp cut-off at a density threshold of $\delta = -0.8$, interestingly close to the density of a spherically symmetric shell-crossing void in an Einstein–de Sitter (EdS) universe.[4] It forms a powerful confirmation of the power of DTFE to reconstruct the density distribution in void regions.

It is particularly informative to compare the DTFE density PDF with that of the linear density field reconstruction from Branchini et al. (1999), who used a rigid grid-based interpolation scheme (CIC; Hockney & Eastwood 1988). The dashed lines in the lin–lin and lin–log diagrams in Fig. 6 are the corresponding PDFs. Several telling differences between the DTFE and PSCz density maps of Branchini et al. (1999) can be identified. The grid-based reconstruction used by the latter yields significantly lower density values in void regions, in the order of $\delta \approx -1$. It is an expression of the inability of the rigid grid-based interpolation to recover meaningful density values as a result of the sparsity of sample points: when no points are found within the grid kernel, the method yields a zero-density value. On the side of the high-density values we see that DTFE recovers systematically higher density values. This is a consequence of the DTFE ability to trace the density field into the most compact and/or highest density regions, without smearing these region out as in the case of rigid kernel procedures. One may of course argue that it would be more appropriate to compare the DTFE results with a correspondingly smoothed CIC field. However, here we seek to highlight the fact that DTFE does not need any such user-specified tuning and does achieve the required filtering automatically.

[4] The theoretical expectation for a mature and shell-crossing void, with a characteristic inverse top-hat density profile, is an underdensity of $\Delta \approx -1 + (1/1.7)^3 \approx -0.8$.

6 PSCz: THE DTFE COSMIC FLOW FIELD

The DTFE reconstruction of the continuous volume-weighted DTFE velocity field of the PSCz catalogue proceeded along the steps outlined in Section 3.6. Because the input velocities have been linearized prior to the DTFE processing there is an implicit limit on the resolution of the reconstructed flow field rendering additional smoothing unnecessary. It also means that one cannot recover features in the flow field on a scale smaller than the kernel size ($\sqrt{5}\,h^{-1}$ Mpc for $r \lesssim 50\,h^{-1}$ Mpc, $\propto l(r)/\sqrt{5}h^{-1}$ Mpc for $r \gtrsim 50\,h^{-1}$ Mpc).

6.0.1 *The supergalactic plane*

Fig. 5 presents the resulting velocity field by means of the projected velocity vectors within the Z-supergalactic plane, superposed upon the corresponding DTFE density contour maps. The length of the velocity arrows can be inferred from the arrow in the lower left-hand corner, which corresponds to a velocity of 650 km s^{-1}.

The processed DTFE velocity field reveals intricate details along the whole volume. The first impression is that of the meticulously detailed DTFE flow field, marked by sharply and clearly defined flow regions over the whole supergalactic plane. Large-scale bulk flows, distorted flow patterns such as shear, expansion and contraction modes of the velocity field are clear features uncovered by our DTFE technique. DTFE recovers clearly outlined patches marked by strong bulk flows, regions with characteristic shear flow patterns around anisotropically shaped supercluster complexes, radial inflow towards a few massive clusters and, perhaps most outstanding, strong radial outflows from the underdense void regions.

The map of Fig. 5 shows the success of DTFE in converting a sample of discretely sampled velocities into a sensible volume-covering flow field. In particular its ability to interpolate over the low-density and thus sparsely sampled regions is striking: the voids show up as regions marked by a near-spherical outflow. By contrast, more conventional schemes, such as TSC or SPH (see Romano-Díaz 2004; Schaap & van de Weygaert 2007), meet substantial problems in defining a sensible field reconstruction in low-density regions without excessive smoothing and thus loss of resolution. At the same time, the local nature of the DTFE interpolation guarantees a highly resolved flow field in high-density regions.

Overall, there is a tight correspondence with the large-scale structures in the underlying density distribution. While the density field shows features down to a scale of $\sqrt{5}\,h^{-1}$ Mpc (within the inner $50\,h^{-1}$ Mpc), the patterns in the flow field clearly have a substantially larger coherence scale, nearly all in excess of $10\,h^{-1}$ Mpc. Of course, a strong correlation between density and velocity fields is to be expected given the artificial origin of the sample velocities as they were generated from the galaxy redshift distribution through the linearization procedure. Strictly speaking this concerns linear features, although it is interesting to see that the correspondence remains almost unanimous for mild non-linear supercluster and void region. The DTFE velocity flow sharply follows the elongated ridge

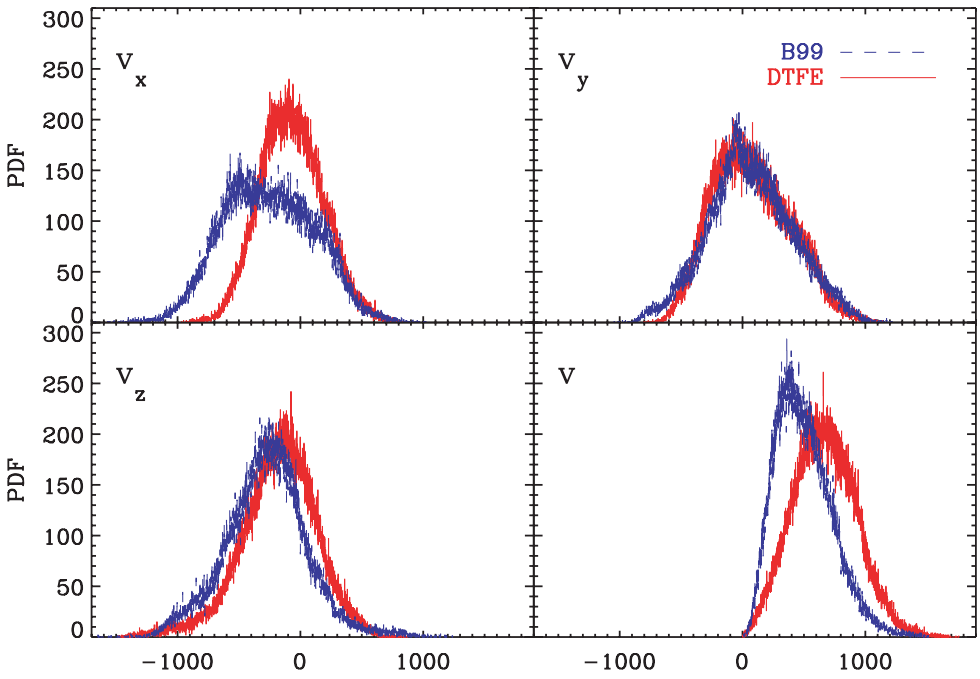

Figure 7. PDFs for the three Cartesian velocity components and velocity amplitude. The red PDFs correspond to those computed by means of the DTFE technique. The blue PDFs are those from Branchini et al. (1999).

of the Pisces–Perseus supercluster. In addition we find the DTFE velocity field to contain markedly sharp transition regions between void expansion and the flows along the body of a supercluster. We should bear in mind that this mainly concerns the outline of features in the velocity flow, the corresponding velocity values remain linear in character. The latter is an artefact of the (artificial) linearization origin of the galaxy velocities in our sample.

Massive bulk motions are particularly concentrated near and around the massive structure extending from the Local Supercluster (centre map) towards the GA region and the Shapley concentration. The DTFE map nicely renders this pronounced bulk flow towards the Hydra–Centaurus region and shows that it dominates the general motions at our Local Group and Local Supercluster. The most massive and coherent bulk flows in the supergalactic plane appear to be connected to the Sculptor void and the connected void regions (towards the left-hand side of the figure). They are the manifestation of the combination of gravitational attraction by the heavy matter concentration of the Pavo–Indus–Telescopium complex, the more distant 'Hydra–Centaurus–Shapley ridge', and the effective push by the Sculptor void region. Conspicuous shear flows can be recognized along the ridge defined by the Cetus wall towards the Pisces–Perseus supercluster ([SGX, SGY] $\approx [20, -40]\,h^{-1}$ Mpc). A similar strong shear flow is seen along the extension of the Hydra–Centaurus supercluster towards the Shapley concentration.

The influence of the Coma cluster is beautifully outlined by the strong and near perfect radial infall of the surrounding matter, visible at the top centre of Fig. 5. Also the velocity field near the Perseus cluster, in the Pisces–Perseus supercluster region, does contain a strong radial inflow component.

Perhaps most outstanding are the radial outflow patterns in and around voids. The intrinsic suppression of shot-noise effects through the adaptive spatial interpolation procedure of DTFE highlights these important components of the Mpc flow field and emphasizes the dynamical role of voids in organizing the matter distribution of the large-scale cosmic web.

6.1 Velocity field: probability distribution function

We have also compared the PDFs of the Cartesian velocity components and the total velocity amplitude. The red PDFs in Fig. 7 represent those computed by means of the DTFE technique, while the blue ones are those from Branchini et al. (1999).

The DTFE velocity PDFs have a healthy Gaussian appearance, as we might have expected for a near linear velocity field. In this respect it is interesting to note the stark differences between the DTFE distribution functions and those of the velocity field of Branchini et al. (1999). In particular the velocity component in the x direction shows a marked deviation. We traced the differences back to the low-density regions, where rigid grid-based methods have considerable difficulty in defining reasonable density values. On the other hand we also note significant differences in the high-density regions. Grid-based methods are unable to resolve these and tend to average the velocities in these regions over the volume of a grid cell. This is reflected in the PDF of the velocity amplitude: the DTFE PDF testifies considerably higher velocities in the DTFE velocity field. Note that this may yield important implications for the analysis of large-scale bulk flows within the sample's volume; conventional methods may yield unjustifiably biased values.

6.1.1 The spatial flow field

It remains a rather challenging task to visualize a 3D flow field. We chose to show the spatial structure of the DTFE rendered velocity flow within the PSCz volume within the three mutually perpendicular central slices through the centre of the supergalactic plane (i.e. the Local Group's location). The combination of the velocity flow within the $2.5\,h^{-1}$ Mpc thick slices along the XY, the XZ and the YZ supergalactic plane provides a reasonable impression of the spatial flow field. To understand its connection with the underlying matter distribution we also depict the density distribution within the same planes.

To appreciate the structure of the PSC*z* velocity flow and to obtain an impression of the density and velocity field contributions on different scales we have included the complementary set of maps in Figs 8 and 9. By means of a set of 3 × 2 frames, the latter shows the density and velocity fields are filtered on a scale of $R_G = 12\,h^{-1}$ Mpc, the former on $R_G = 3.8\,h^{-1}$ Mpc. The density field in the *XY*, *XZ* and *YZ* central slices is represented by grey-scale maps in three consecutive rows of the left-hand column, the grey-scale values in all three frames are scaled according to the values in the bar atop the figure. The corresponding velocity vector maps are shown in the right-hand column. The velocity vectors in the three planes are normalized such that the reference velocity vector depicted atop the three frames corresponds to 650 km s^{-1}. The view on a scale of $R_G = 12\,h^{-1}$ Mpc is that of the large-scale (linear) contributions to the flow field and identifies the agents of these large-scale flows. The considerably more detailed map of Fig. 8 has the intention of identifying the imprint of mild non-linear structural features such as superclusters and voids on the corresponding velocity flow.

The combination of Figs 8 and 9 is a potentially rich source for the study of the structural dynamics in the local Universe. Important for the present study is that it emphasizes three key issues of the DTFE velocity field analysis.

(i) The spatial adaptivity of DTFE allows the resolution of the velocity flow in and around non-linear features in the density field.

(ii) The spatial adaptivity of the DTFE kernel to the density of sample points implies a dependence of the spatial resolution of the (raw) DTFE velocity field on the sampling density. As a result high-resolution maps do involve a rather inheterogeneous spatial resolution over the sample volume.

(iii) The DTFE velocity field has a more homogeneous resolution than the corresponding density field. This is a result of the larger scale character of cosmic velocity fields.

7 DTFE MAPS: SPATIAL RESOLUTION

The cosmic matter distribution and cosmic velocity flows include contributions over a wide range of scales. One of the virtues of DTFE is its large dynamic range, a result of its adaptivity (see Schaap & van de Weygaert 2007). In principle we are therefore equipped for an assessment of the structure of the produced DTFE PSC*z* density and velocity maps in terms of their structure at various scales. However, before doing so we need to pay attention to the fact that for the flux-limited sample the DTFE maps do not necessarily involve a homogeneous resolution.

7.1 Heterogeneous versus homogeneous resolution

The cosmographical presentation of the pure DTFE density and velocity maps in Fig. 5 in Section 5.1 does not include the issue of its rather non-uniform, radially declining, spatial resolution. This issue becomes prominent in the comparison between the maps of Fig. 9 and those of Fig. 8. While the latter have a uniform but low spatial resolution of $R_G = 12\,h^{-1}$ Mpc, the higher resolution maps filtered on a scale $R_G = 3.8\,h^{-1}$ Mpc do lack such uniform resolution.

By its nature, DTFE resolves regions of a higher sampling density on a finer scale, as can be readily inferred from the structure of the Delaunay grid in Fig. 3. As a result the spatial resolution diminishes when the intergalaxy separation in the sample increases. The increase of the PSC*z* intergalaxy separations as a function of distance (Fig. 2) thus provides an order-of-magnitude estimate of the effective resolution scale as function of radial distance from the Local Group.[5]

A resolution scale of $R_G \sim 3.8\,h^{-1}$ Mpc corresponds to a radial depth of $\sim 30\,h^{-1}$ Mpc while $R_G \sim 12\,h^{-1}$ Mpc is reached at a distance of $120\,h^{-1}$ Mpc. By implication the maps in Fig. 8 are uniform in the inner $30\,h^{-1}$ Mpc, but they are marked by a gradually diminishing spatial resolution at larger distances. These are in particular the density maps which show the gradually fading resolution of the $3.8\,h^{-1}$ Mpc maps most clearly. By contrast, the $R_G = 12\,h^{-1}$ Mpc maps show a uniformly resolved view of the structure and flow in the local Universe. A scale of $R_G = 12\,h^{-1}$ Mpc corresponds to the sample intergalaxy distance at the outer edge of the PSC*z* sample.

For a proper quantitative analysis and assessment of the DTFE density and velocity field reconstructions it is of the utmost importance to take into account the gradually diminishing spatial resolution of the raw DTFE maps. In this respect we also need to take into account that cosmic density and velocity fields are composed of contributions from a range of scales. By implicitly filtering out small-scale contributions in regions with a lower sampling density DTFE will include a smaller range of spatial scales contributing to a field reconstruction. On average, they will therefore correspond to regions with a lower amplitude, a subtle point of importance in any quantitative analysis. A comparison of DTFE density and velocity maps in the PSC*z* volume shows that the latter seems to be hardly affected by this effect, a manifestation of the fact that the cosmic velocity field is dominated by larger scale modes than the density field (Peebles 1980).

7.1.1 The large-scale local Universe: the $12\,h^{-1}$ Mpc maps

In the large-scale $R_G = 12\,h^{-1}$ Mpc density and velocity fields of Fig. 9 we recognize nearly all features of the previous discussion on the structure of the supergalactic plane (Section 5.1). The *XY* supergalactic plane clearly involves a local matter concentration: while the *XY* plane represents a more or less even distribution of in particular high-density features, we observe a concentration of high-density regions towards the corresponding $Z = 0$ axis in the *XZ* density map and a more moderate density distribution with some occasional high-density patches in the *YZ* map. One of the most conspicuous mass concentrations in the latter is the Coma cluster, at around [SGY, SGZ] $\approx [70, 0]\,h^{-1}$ Mpc, embedded within a massive 'Great Wall' complex extending along the *Z*-axis. It clearly emphasizes the moderate density values near our own Local Supercluster, lying in between the massive Hydra–Centaurus–Shapley concentration and the Pisces–Perseus concentration in the *XY* plane. The only massive feature which had not been traced in the *XY* map is the concentration near [SGY, SGZ] $\approx [-40, -100]\,h^{-1}$ Mpc.

The presence of massive matter concentrations in the $R_G = 12\,h^{-1}$ Mpc map induces strongly correlated patterns in the flow field. The *XZ* map is dominated by a strong and rather coherent flow towards the $Z = 0$ (*XY*) supergalactic plane. Interesting is to see that this flow is tied in with an almost equally prominent outflow from the low-density regions towards the upper right-hand side of the maps. A similar pattern can be recognized in the *YZ* map, where near the centre we observe an equally massive flow towards the supergalactic $Z = 0$ plane. It appears to be coupled to a truly massive radial outflow from the underdensity near [SGY, SGZ] $\approx$ [0, 80] h^{-1} Mpc. If anything, this demonstrates the key role of

[5] Note that the resolution scale is not exactly a function of radial distance, it is entirely determined by the local sampling density. On average this does increase as function of radial distance. See Fig. 3.

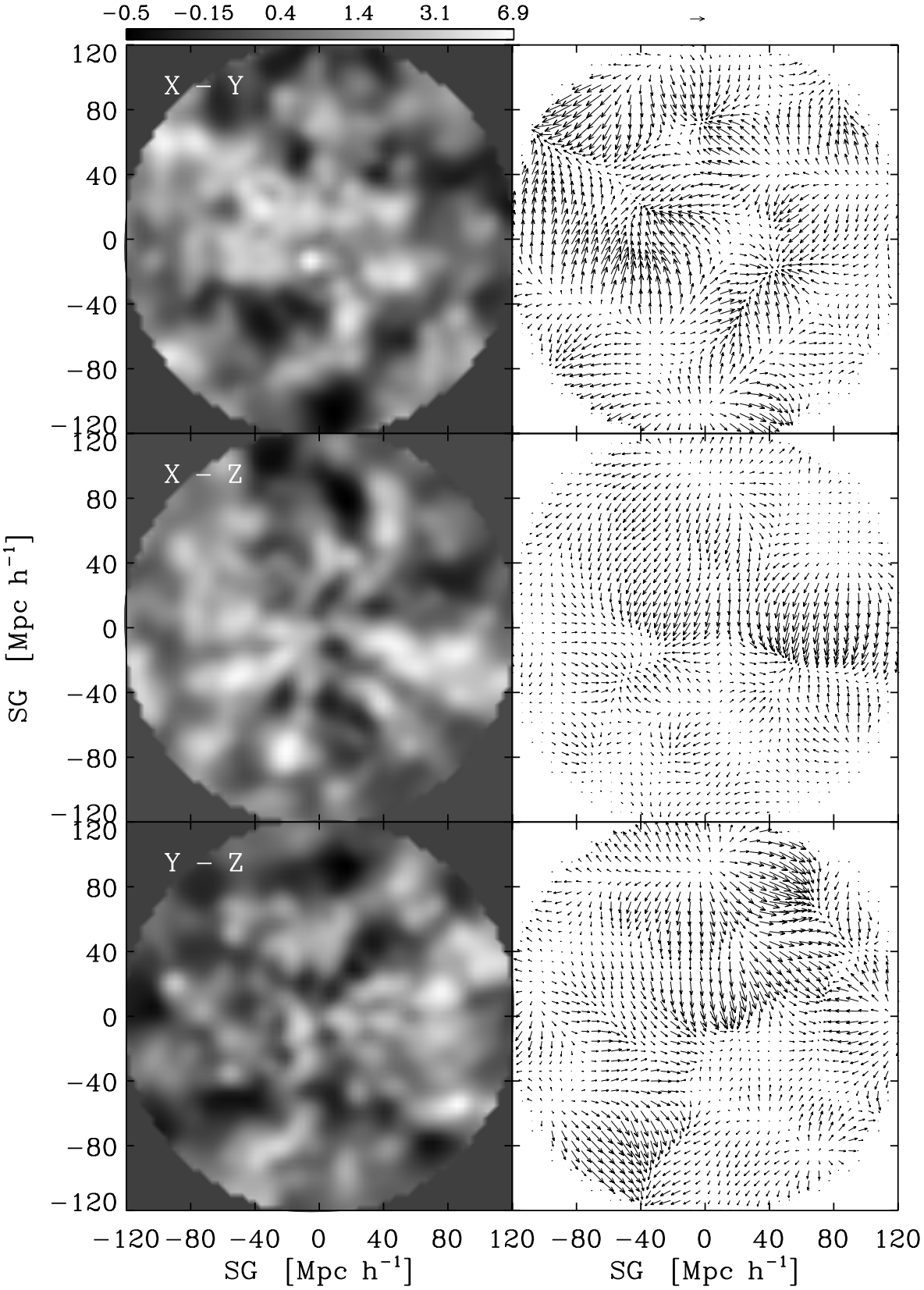

Figure 8. The DTFE density (left-hand column) and velocity vector (right-hand column) maps of the PSCz sample in three mutually perpendicular central supergalactic planes: the *XY*, *XZ* and *YZ* planes (from top to bottom). The density and velocity fields are smoothed on a scale of $3.8\,h^{-1}$ Mpc. This implies a uniform resolution up to a radius of $30\,h^{-1}$ Mpc around the centre, with a gradually diminishing resolution towards the outer edge of the sample volume. The grey-scale bar at the top left-hand side indicates the density values. The velocity vectors are scaled such that the vector atop the figure corresponds to 650 km s^{-1}.

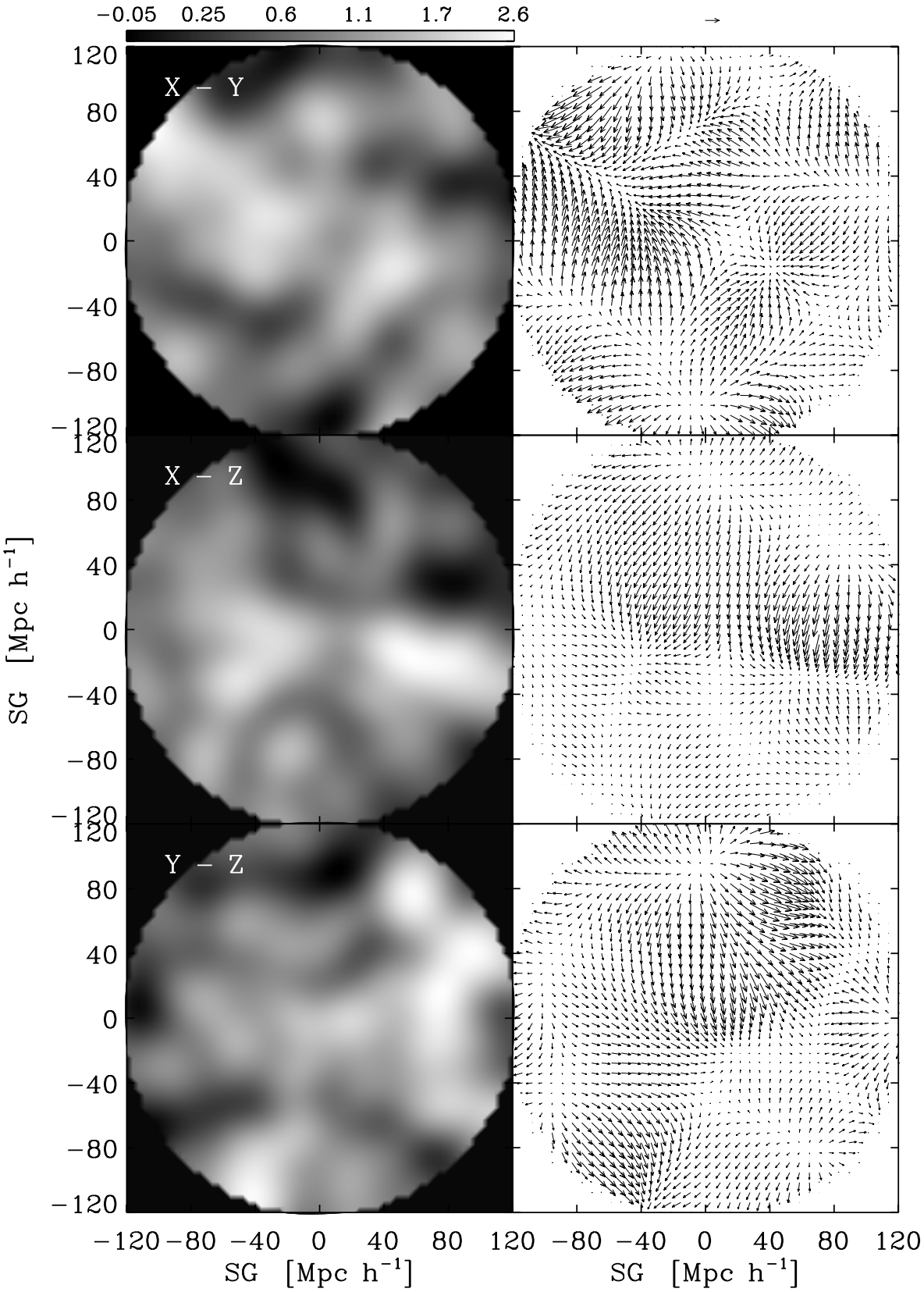

Figure 9. The DTFE density (left-hand column) and velocity vector (right-hand column) maps in three mutually perpendicular central supergalactic planes: the *XY*, *XZ* and *YZ* planes (from top to bottom). The density and velocity fields are smoothed on a scale of $12\,h^{-1}$ Mpc, involving a uniform resolution over the sample volume. The grey-scale bar at the top left-hand side indicates the density values. The velocity vectors are scaled such that the vector atop the figure corresponds to 650 km s^{-1}.

low-density regions in the dynamics of the local Universe, and in the formation of cosmic structure in general.

Within the *XY* supergalactic plane we recognize the familiar flow patterns discussed in Section 5.1 – the coherent bulk flow along the Local Supercluster–Centaurus–Shapley axis. It is coupled to coherent towards the Pisces–Perseus region, via a saddle point near the Local Group location: the dominant shear flow in the local Universe. Radial outflow low-density regions are somewhat less prominent; the outflow from the local Sculptor void appears to be merged into a large-scale coherent bulk flow.

7.1.2 Flow field scale dependence: 3.8 h^{-1} Mpc versus 12.0 h^{-1} Mpc

The impact of DTFE is particularly emphasized by the comparison of the medium-resolution $3.8\,h^{-1}$ Mpc maps and the $12.0\,h^{-1}$ Mpc maps. The more detailed density map of the maps in Fig. 8 reveals considerably more detail in both density and velocity maps.

The structure in the *XY* density map has already been discussed in detail in Section 5.1. For the $R_{\rm G} = 3.8\,h^{-1}$ Mpc density there are two major points of importance in comparison to the $R_{\rm G} = 12\,h^{-1}$ Mpc maps. The first is the gradually decreasing density values towards the outer regions: most prominent features are concentrated within the inner $30{-}40\,h^{-1}$ Mpc radius. This is a direct consequence of the decreasing spatial resolution of the non-uniform $R_{\rm G} = 3.8\,h^{-1}$ Mpc maps (see Section 7). Another feature of interest is the more prominent presence of (deeper) void regions with respect to the corresponding $R_{\rm G} = 12\,h^{-1}$ Mpc map. This is in particular true for the *YZ* plane.

The $R_{\rm G} = 3.8\,h^{-1}$ Mpc velocity field stands out by considerably more sharply defined and outlined features. All features that were recognized in the $R_{\rm G} = 12\,h^{-1}$ Mpc velocity field can also be identified, be it they are much more sharply defined. Moreover, all over the volume these sharp velocity features are clearly correlated with features in the density field. The mild non-linear nature of supercluster complexes is reflected in pronounced bulk and shear flows. In the velocity map these often go along with remarkably sharply defined transition regions where the flow changes abruptly as it encounters a flow from another direction. Also void outflows appear to be much more prominent than the weakly positive divergence regions in the large-scale map. The DTFE void outflows have the appearance of superhubble bubbles, and relate very well to the deep non-linear potential wells of true voids (see Schaap & van de Weygaert, in preparation). In addition, we can recognize small-scale non-linear features that were not seen in the $R_{\rm G} = 12\,h^{-1}$ Mpc velocity map. The radial infall towards Coma and the radial outflow out of the Sculptor void are telling examples.

Both aspects strongly underline the ability of DTFE to trace velocity flows into non-linear regions. This forms a strong argument for DTFE's potential in the analysis of the dynamics of mild non-linear structures, such as filamentary or wall-shaped superclusters and voids. The DTFE analysis of Virgo cold dark matter simulations by Schaap & van de Weygaert (in preparation) does indeed provide quantitative evidence for this ability of DTFE. Only when the non-linear evolution of a structure has proceeded towards a higher non-linear stage, marked by multistream regions and shell-crossing displacements, the linear interpolation scheme of DTFE will break down.

8 INDIVIDUAL COSMIC STRUCTURES

The ability of the DTFE method to resolve and identify both small- and large-scale features, on the condition of being sufficiently sampled, makes it into a highly promising basis for the development of structure detection algorithms.

To illustrate the variety of structures that may be identified by DTFE we zoom into four different regions of the DTFE PSC*z* map, each of a different character. The four regions are the Local Supercluster, the Coma cluster, the Sculptor void and the Pisces–Perseus and Cetus supercluster filament. The four corresponding panels in Fig. 10 show the density field and corresponding velocity field vectors. To ascertain optimal resolution the density field has been smoothed with a Gaussian kernel of a mere $1\,h^{-1}$ Mpc. It is important to realize that as a result of the irregular spatial resolution this does not necessarily mean that all structures of that size are revealed. Note that the physical size of the corresponding panels varies with the spatial extent of the depicted structure.

8.1 The Local Supercluster

The top left-hand panel shows the complex velocity field in and around the Local Supercluster. The Virgo cluster is located just above the Local Group. Particularly prominent is the presence of the GA region and its dominant influence on the velocity field. At the location of the Local Group ([SGY, SGZ] $\approx$ [0, 0] h^{-1} Mpc) we find a large bulk flow, part of a large-scale shear flow towards the GA region. The shear patterns is a result of the exerted gravitational influence of the GA and Pisces–Perseus supercluster (e.g. see Romano-Díaz 2004).

8.2 The Pisces–Perseus supercluster

The bottom right-hand frame focuses on the Pisces–Perseus supercluster and the Cetus wall. The prominent flow along the Pisces–Perseus chain towards the Cetus wall is a clear indication of the dynamical connection between these two structures. Their gravitational influence can be traced along the whole zoomed region. The velocity field around the underdense region located at [SGX, SGY] $\approx$ [45, -60] h^{-1} Mpc is strongly distorted by these two massive structures. Note the presence of the shear pattern near the top left-hand corner, near the location of the Local Group.

8.3 The coma cluster

The top right-hand panel shows how the Coma cluster, embedded within the Coma wall, distorts the velocity field in its surroundings. The DTFE reconstruction clearly depicts the almost isotropic infall into the Coma cluster. The slight offset is an artefact of our implementation of the DTFE interpolation towards the image grid locations. Coma is embedded within the Coma wall. The shear pattern visible near the bottom left-hand side is the result of the opposing forces between the Coma region and the Local Supercluster region.

8.4 The Sculptor void

The Sculptor void and surroundings is the subject of the bottom left-hand frame. The lowest measured DTFE density contrast value (smoothed at $1\,h^{-1}$ Mpc) in this region is ≈ -0.78 at the deepest of the void. At the smoothed scale of $\sqrt{5}h^{-1}$ Mpc the DTFE density threshold is -0.74, in agreement with the reported value by Plionis & Basilakos (2002) of -0.69. The velocity field of this almost 'empty' expanding region is distorted by the surrounding matter distribution. Small, yet detectable, distortions delineate the

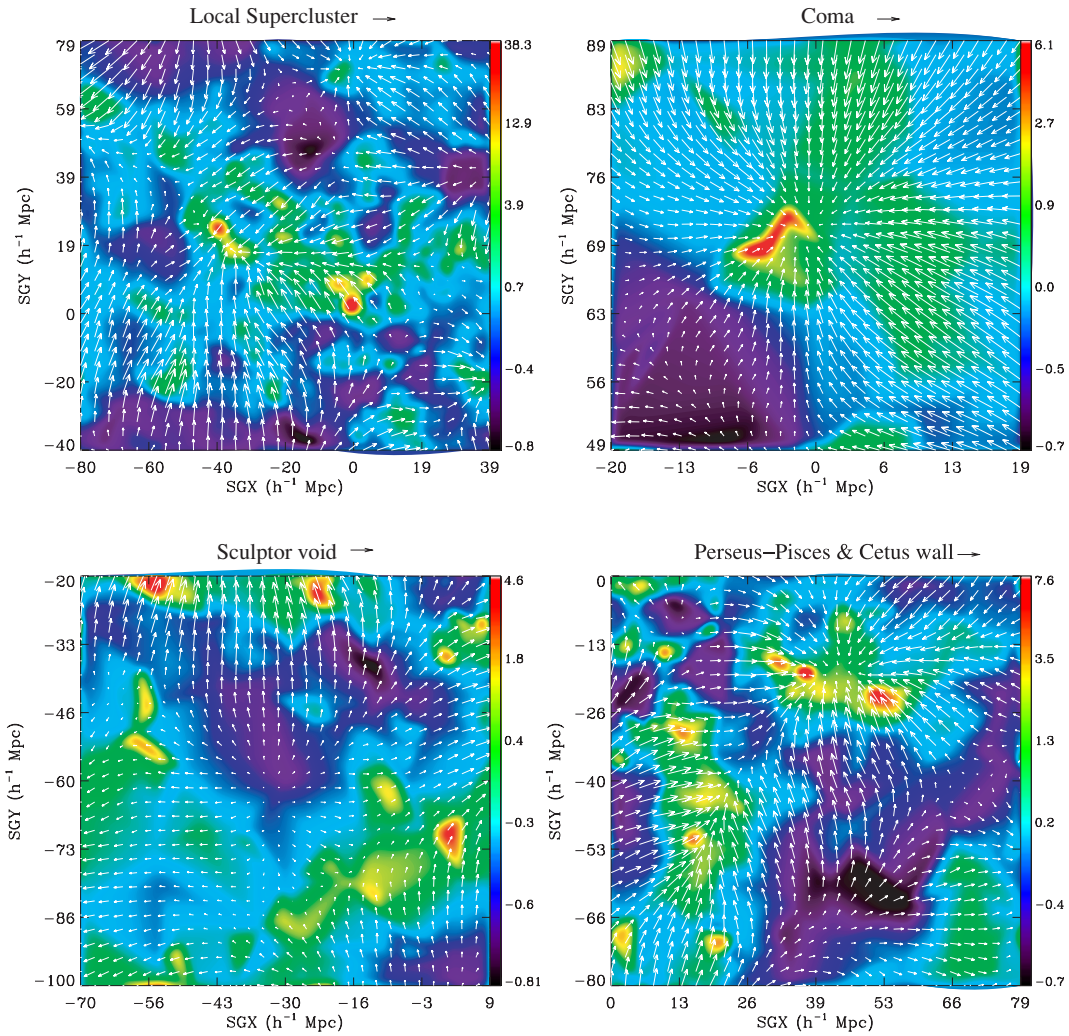

Figure 10. Density and velocity zooms for four different regions along the supergalactic plane indicated by the labels at the top of each frame. The density field has been convolved with a Gaussian kernel of $1\,h^{-1}$ Mpc for a better impression of such field. Note that the density colour contour values in each of the frames are chosen differently, their scaling reflected in the colour bars at the right-hand side of each frame. The velocity vectors at the top of each frame, at the right-hand side of the frame's name, correspond to a velocity of 650 km s^{-1}.

boundary of this void with the surrounding matter distribution, i.e. the Sculptor wall.

9 THE DTFE PSC*z* VELOCITY DIVERGENCE

A direct spin-off of the DTFE velocity field analysis is that it implicitly comes along with the velocity field divergence, shear and vorticity. In the outline of the DTFE method, in Section 3.6, we described how the DTFE method determines the gradient $\widehat{\nabla f}|_m$ of the sample field f in each Delaunay simplex m (equation 3). For the three spatial components of the velocity field, (v_x, v_y, v_z), this translates into a velocity gradient counting nine components $\partial v_i/\partial x_j$ (equation 9). Within the context of DTFE each velocity gradient $\partial v_i/\partial x_j$ has a uniform value within each Delaunay tetrahedron. By implication, the reconstructed DTFE velocity *gradient* field is not continuous.

9.1 Velocity divergence, shear and vorticity

From the nine velocity gradient components $\partial v_i/\partial x_j$ we can directly determine the three velocity deformation modes, the velocity divergence $\nabla \cdot \boldsymbol{v}$, the shear σ_{ij} and the vorticity $\boldsymbol{\omega}$,

$$\nabla \cdot \boldsymbol{v} = \left(\frac{\partial v_x}{\partial x} + \frac{\partial v_y}{\partial y} + \frac{\partial v_z}{\partial z} \right) ,$$

$$\sigma_{ij} = \frac{1}{2} \left\{ \frac{\partial v_i}{\partial x_j} + \frac{\partial v_j}{\partial x_i} \right\} - \frac{1}{3} (\nabla \cdot \boldsymbol{v}) \, \delta_{ij} ,$$

$$\omega_{ij} = \frac{1}{2} \left\{ \frac{\partial v_i}{\partial x_j} - \frac{\partial v_j}{\partial x_i} \right\} , \qquad (10)$$

where $\boldsymbol{\omega} = \nabla \times \boldsymbol{v} = \epsilon^{kij} \omega_{ij}$ (and ϵ^{kij} is the completely antisymmetric tensor). In the theory of gravitational instability, there will be no vorticity contribution as long as there has not been shell crossing (i.e. in the linear and mild non-linear regime). For the evolution of density perturbations, the velocity divergence is an important velocity field component from the early linear regime onward. As non-linearity sets in the deforming character of accompanying shear flows become increasingly decisive in shaping the cosmic matter distribution. It is in particular via the Zel'dovich formalism (Zel'dovich 1970) and the *cosmic web* theory by Bond and collaborators that we have come to

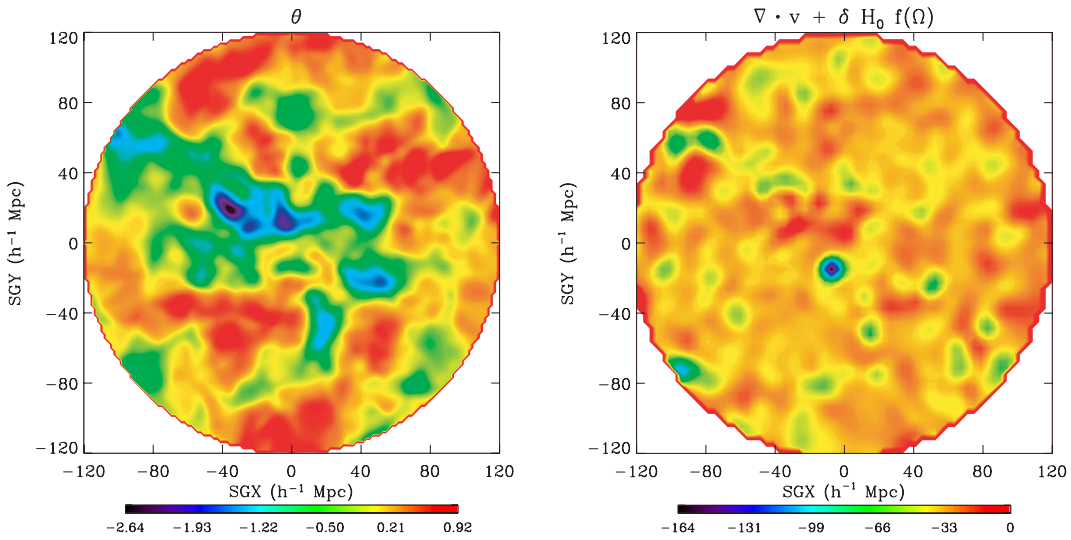

Figure 11. Left-hand column: DTFE velocity divergence field, on a smoothing scale of $R_G = \sqrt{5}h^{-1}$ Mpc projected along the Z-supergalactic plane. The thin slice corresponds to the one presented in Fig. 5. The velocity divergence is in units of the Hubble parameter H_0. The colour bar represents the scale of the plotted velocity divergence. Right-hand column: The map, along the Z-supergalactic plane, of the difference between the DTFE velocity divergence field and the linear theory prediction for the corresponding DTFE density field. The colour bar indicates the corresponding field values, in units of km s^{-1} Mpc^{-1}.

appreciate the key role of tides and velocity shear in the formation of the observed web-like Mpc matter distribution (Bond et al. 1996).

The relationship between the cosmic density field on one hand and the velocity divergence and shear fields on the other hand contains substantial information on the dynamics and formation of structure in the universe. Within the context of the corresponding DTFE analysis it is important to realize that there is an important and implicit discrepancy: the DTFE density and velocity fields are entirely continuous. The velocity divergence fields consist of discontinuous patches: the Delaunay tetrahedra, each with a constant value of $\nabla \cdot \boldsymbol{v}$. This renders a perfect one-to-one correspondence between the raw DTFE density and $\nabla \cdot \boldsymbol{v}$ fields is unfeasible. Filtering over the scale of a Delaunay simplex is usually necessary to restore the physically expected relations.

In the following subsections we present the maps of the velocity divergence field and the velocity shear field in the same central supergalactic planes as in Figs 5 and 8. By smoothing the velocity divergence, velocity shear and vorticity fields with the Gaussian kernel $R_G = \sqrt{5}h^{-1}$ Mpc, akin to the density map in Figs 5 and 9, we restore a sense of continuity to the resulting maps.

9.2 The DTFE velocity divergence map

The DTFE normalized velocity divergence estimate $\widehat{\theta}$ is the sum of the trace of the DTFE velocity-gradient components,

$$\widehat{\theta} \equiv \frac{\widehat{\nabla \cdot \boldsymbol{v}}}{H_0} = \frac{1}{H_0}\left(\widehat{\frac{\partial v_x}{\partial x}} + \widehat{\frac{\partial v_y}{\partial y}} + \widehat{\frac{\partial v_z}{\partial z}}\right), \tag{11}$$

with H_0 the Hubble constant.[6] In Fig. 11 (left-hand column) we have plotted $\widehat{\theta}$. Its full spatial structure at two different resolutions is shown in Fig. 12.

The expanding and contracting modes of the velocity field are clearly delineated. Expanding regions, corresponding with or surrounding large and deep underdense voids, are identified as those with red to yellow tones marking positive divergence modes. The Sculptor and Fornax voids and the underdense regions around the Coma cluster can be immediately recognized. Other conspicuous expanding regions are that near the Camelopardalis cluster, located at [SGX, SGY] $\approx$ [40, 45] h^{-1} Mpc, and the one at the right-hand side of the Cetus wall at [SGX, SGY] $\approx$ [50, -55] h^{-1} Mpc.

The regions with a negative divergence are contracting, matter is falling in along one or more directions. The strongest contractions, represented by the blue tones, are related to the peaks in the density field which can be immediately identified with the most massive structures located along this slice. The Hydra–Centaurus supercluster is the most prominent region of infall. Easily recognizable are all clusters such as the Virgo, Camelopardalis and Coma cluster, the Pisces–Perseus supercluster, the Cetus wall, the Pavo–Indus–Telescopium complex, and partly also the Shapley concentration. These high-contrast blue regions are embedded within regions with more moderate infalling motions. These regions, with green contour values, have densities slightly in excess of the mean. They outline a percolating region with a roughly filamentary shape.

In the interpretation of the velocity divergence map it is crucial to take account of an important artefact: high amplitudes of the velocity divergence are seemingly concentrated in the inner region of the PSCz volume. This can be understood on the same grounds as a similar tendency for the density field, the lack of small-scale power in the outer regions as a result of the diminishing sampling density. A correction for this effect is only possible on the basis of a cosmological model assumption and does not fall within the context of this study.

9.3 The density–velocity divergence relation

The velocity divergence and the density contrast are related via the continuity equation (Peebles 1980). In the linear regime this is a strictly linear one-to-one relation,

$$\frac{1}{H}\nabla \cdot \boldsymbol{v}(\boldsymbol{x}, t) = -\frac{f(\Omega_m)}{b}\, a(t)\, \delta(\boldsymbol{x}, t)\,, \tag{12}$$

[6] We have adopted a value of $h = 0.7$ ($H_0 \equiv 100\, h\, \mathrm{km\, s^{-1}\, Mpc^{-1}}$).

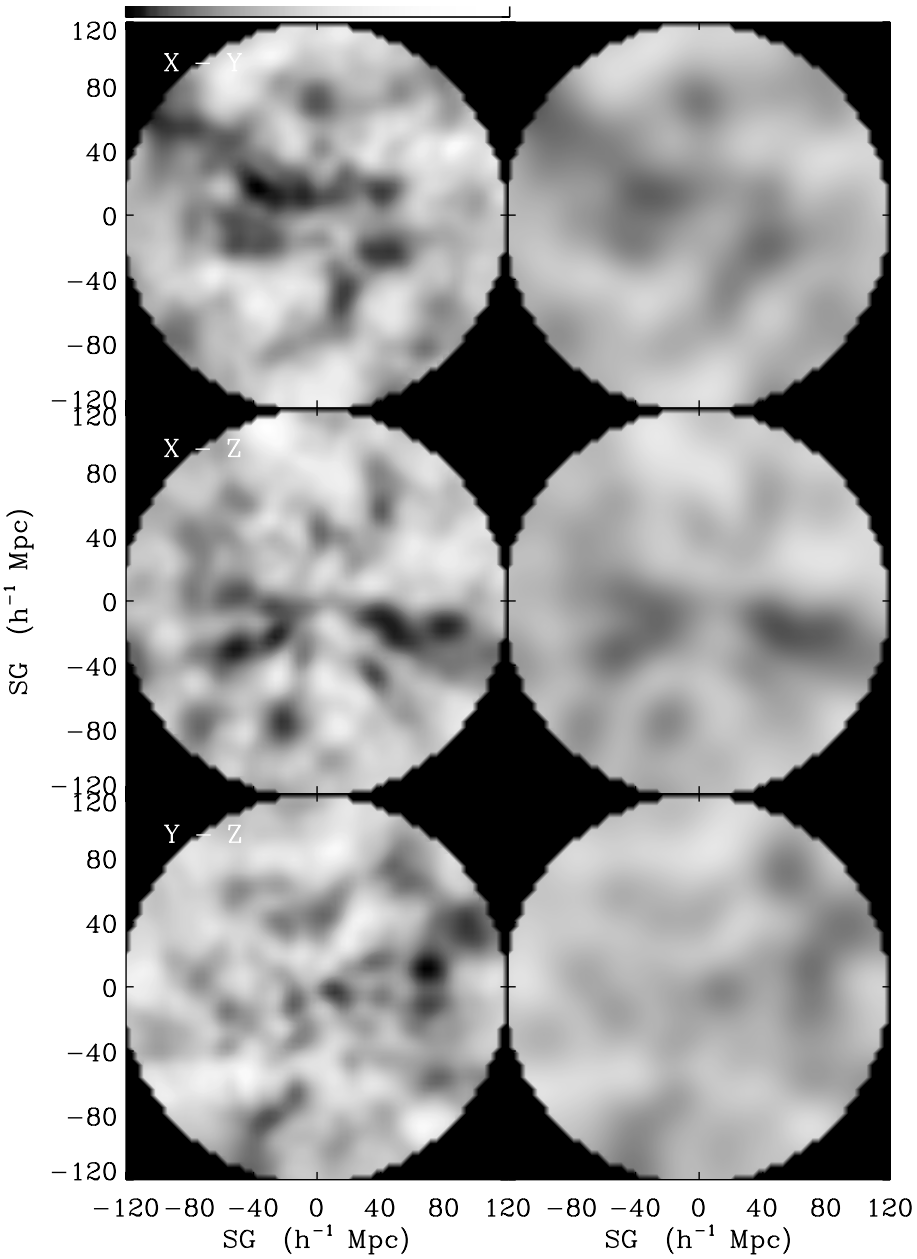

Figure 12. The DTFE velocity divergence field on a smoothing scale of $3.8\,h^{-1}$ Mpc (left-hand column) and $10\,h^{-1}$ Mpc (right-hand column). The maps in the consecutive rows concern the three mutually perpendicular central supergalactic planes: the *XY*, *XZ* and *YZ* planes (from top to bottom). Note that the map on a scale of $3.8\,h^{-1}$ Mpc is uniform only out to a radius of $30\,h^{-1}$ Mpc, with a gradually diminishing resolution towards the outer edge of the sample volume. Also compare the images with the density fields in Figs 8 and 9, they are approximately the negatives of the corresponding density fields. The grey-scale values are in units of the Hubble parameter H_0, with their values given in the bar at the top of the figure.

linking the (galaxy) density perturbation field δ to the peculiar velocity field $\boldsymbol{v}$ via the factor $f(\Omega_{\rm m})$ (see Peebles 1980). In this we take into account that our discussion concerns the density field as sampled by galaxies, whose distribution is supposed to be linearly biased with respect to the underlying matter density. There remains a one-to-one relation between velocity divergence and density into the mild non-linear regime (see equation 13), which explains why the map of the velocity divergence (11) is an almost near perfect negative image of the density map (see Fig. 5).

The approximate validity of the linear divergence–density relation (12), on a scale of $R_{\rm G} = \sqrt{5}\,h^{-1}$ Mpc, over the PSCz volume can be appreciated from the contour map in the right-hand frame of Fig. 11. The map, in the same supergalactic *XY* plane as in the left-hand frame, shows the difference between the divergence term on the left-hand side of equation (12) and the density term on the right-hand side, in units of km s^{-1} Mpc^{-1}. Evidently, over the entire volume the residual map is near uniform, with the exception of a 'hotspot' near [SGX, SGY] $\approx [-10, -10]\,h^{-1}$ Mpc. If anything, we see a slight tendency for the differences to increase outward. This is most likely to be understood from a different reaction of the velocity field to the diminishing sampling density than the density field.

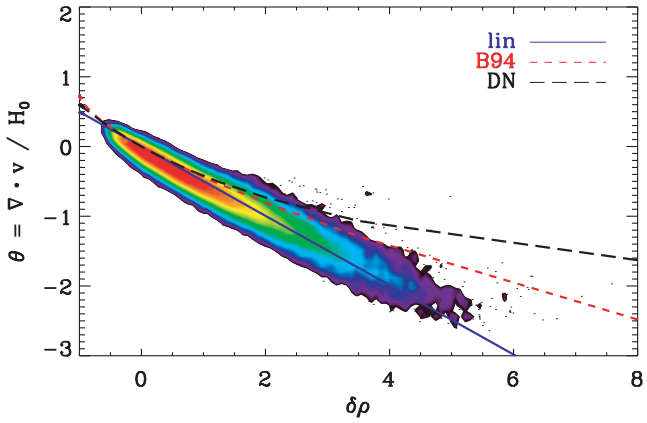

Figure 13. Scatter plot of density versus velocity divergence, in terms of a contour plot of the density of scatter points. The solid line indicates the linear density–velocity divergence relation. Two approximate non-linear relations are also indicated, the short-dashed line depicts the approximation of Bernardeau (1992), the long-dashed one the approximation by Nusser et al. (1991).

The residual map's Fig. 11 impression of near linearity is confirmed by the scatter plot between velocity divergence ($\nabla \cdot \boldsymbol{v}$) and (galaxy) density δ in Fig. 13. The scatter point density in the figure is shown by means of a contour map of the scatter point density.

The scatter plot is compared with three different relations. Superimposed as a solid line is the linear relation, $\nabla \cdot v = -H_0 \beta \delta$. The near perfect linearity of the ($\nabla \cdot \boldsymbol{v}$)-$\delta$ relation reflects the origin of the velocity estimates on the basis of a linearization process. Deviations from linearity, be it minor, are observed only for the lowest and highest density values.

Even in the quasi-linear and mild non-linear regime the one-to-one correspondence between velocity divergence and density remains intact, be it that it involves higher order terms (see Bernardeau et al. 2002, for an extensive review). Within the context of Eulerian perturbation theory Bernardeau (1992) (B) derived an accurate second-order approximation form the relation between the divergence and the density perturbation $\delta(\boldsymbol{x})$. Nusser et al. (1991) (N) derived a similar quasi-linear approximation within the context of the Lagrangian–Zel'dovich approximation. According to these approximate non-linear relations,

$$\frac{1}{H}\,\nabla \cdot \boldsymbol{v}(\boldsymbol{x}) = \begin{cases} \frac{3}{2} f(\Omega_{\rm m}) \left\{ 1 - [1+\delta(\boldsymbol{x})]^{2/3} \right\} & \text{(B)} \\ -f(\Omega_{\rm m})\, \frac{\delta(\boldsymbol{x})}{1+0.18\,\delta(\boldsymbol{x})} & \text{(N)} \end{cases} \tag{13}$$

for a universe with Hubble parameter $H(t)$ and matter density parameter $\Omega_{\rm m}$. For comparison we have also included these approximate relations for mild non-linear density and velocity fields in Fig. 13 (B: the short-dashed line, N: the long-dashed line). These relations are clearly too pronounced for the velocity divergence map of Fig. 11.

9.4 The velocity divergence PDF

The right-hand panels of Fig. 6 show the PDF for the DTFE velocity divergence field. The nice mild non-Gaussian character of the PDF (in the top lin–lin plot) argues for the quality of the DTFE velocity field reconstructions: the DTFE velocity field interpolation scheme is able to recover to considerable accuracy the velocity divergence PDF into the non-linear regime from a discrete particle distribution. It may also be noted that the nice mild non-linear character of the DTFE density and velocity divergence field reconstructions are, at hindsight, an indication for the validity of the 'linearization' procedure of Branchini et al. (1999) into the early non-linear regime.

The velocity divergence PDF forms a near perfect mirror image of the density field PDF (left-hand panel), to be expected on the basis of the continuity equation through which the velocity divergence and the density field are related (see Section 9.3). This relation is reflected in the density and velocity divergence PDFs in the lin–lin plots of the top row and is even more clear when comparing the lin–log equivalents in the bottom row. DTFE is clearly able to sharply follow the velocity divergence distribution, both on the negative velocity divergence side corresponding to infalling motions and on the positive velocity divergence end representative for the outflow from void region.

It forms a contrast to the rather poor correspondence between the density and velocity divergence distributions in the corresponding reconstruction of Branchini et al. (1999): the lin–lin plots show that they do not form each other's mirror image. We may also note that its velocity divergence distribution is considerably broader than that of the equivalent DTFE PDF. This adheres to a known artefact of grid-based velocity field interpolations: implicitly these yield mass-weighted values whose PDFs have wider wings than would be expected for the distribution of proper volume-weighted quantities in the mild non-linear regime (Bernardeau & van de Weygaert 1996).

Bernardeau & van de Weygaert (1996) convincingly demonstrated that the PDF recovered by Delaunay tessellation (i.e. DTFE) interpolation closely adheres to the predictions of Eulerian perturbation theory. The velocity divergence PDF is strongly sensitive to the underlying cosmological parameters, in particular the cosmological density parameter $\Omega_{\rm m}$. By applying DTFE towards determining the velocity divergence PDF this not only implies the possibility to get an accurate estimate of $\Omega_{\rm m}$ but also one which circumvents the usually involved degeneracy between the cosmic matter density $\Omega_{\rm m}$ and the bias b between the matter and galaxy distribution. In a follow-up study (Bernardeau & van de Weygaert 1997) successfully tested this on a range of N-body simulations of structure formation, showing Delaunay interpolation indeed recovered the right values for $\Omega_{\rm m}$.

The sensitivity of the PDF to $\Omega_{\rm m}$ is particularly marked near the peak of the PDF and in the maximum void expansion rate, that is, the maximum value of the velocity divergence $\theta_{\rm max}$. The exact location of the peak also includes a dependence on cosmological scenario and level of non-linearity. To infer $\Omega_{\rm m}$ extra assumptions would need to be invoked. It is more straightforward to read off the value of $\Omega_{\rm m}$ from the characteristic sharp cut-off of the PDF on the side of the positive velocity divergence values. This cut-off relates to the maximum expansion rate of voids, which is predicted to be

$$\theta_{\rm max} = 1.5\,\Omega^{0.6}, \tag{14}$$

in which we ignore the (rather minor) dynamical influence of a cosmological constant. The value of 1.5 is the difference in value of the Hubble parameter in an empty $\Omega = 0$ universe and that in an EdS universe $\Omega = 1$, reflecting the fact that the interior of the deepest voids locally mimic the behaviour of an $\Omega = 0$ universe. Following a related idea Dekel & Rees (1994) obtained a strong lower bound on the value of $\Omega_{\rm m} \sim 0.3$ on the basis of an estimate of the value of expansion rate of the nearby Sculptor void. However, for a proper determination one should seek to carefully recover the sharp cut-off of the PDF. Bernardeau & van de Weygaert (1996) detailed various arguments why a proper determination of the cut-off is non-trivial. They convincingly demonstrated the success of tessellation-based methods in outlining the PDF's sharp edge. Here we infer from the

DTFE-determined PSCz velocity divergence PDF (Fig. 6) that

$$\Omega_{\rm m} = 0.35 \pm 0.04. \quad (15)$$

This value agrees with the value determined on the basis of the PDF's peak (equation 14). The $\nabla \cdot \boldsymbol{v}$ variation within each individual bins is used to obtain the error estimate. Given that the input velocity field has a value of $\beta = 0.5$, that is, $\Omega = 0.315$ and $b = 1$, this forms a confirmation of the ability of DTFE to self-consistently infer the underlying value of cosmological parameters, in particular that of $\Omega_{\rm m}$.

10 VELOCITY SHEAR AND VORTICITY

The map of the amplitude of the shear component in the DTFE velocity field in the supergalactic *XY* plane is shown in Fig. 14. The map shows the DTFE estimate of the amplitude of the shear tensor,

$$\widehat{\sigma} \equiv \Sigma\,(\widehat{\sigma}_{ij}\widehat{\sigma}_{ij})^{1/2}, \quad (16)$$

where $\widehat{\sigma}_{ij}$ is the symmetric traceless part of the DTFE-determined velocity gradient estimate,

$$\widehat{\sigma_{ij}} = \frac{1}{2}\left\{\widehat{\frac{\partial v_i}{\partial x_j}} + \widehat{\frac{\partial v_j}{\partial x_i}}\right\} - \frac{1}{3}\left(\widehat{\nabla \cdot \boldsymbol{v}}\right)\delta_{ij}. \quad (17)$$

Shear flows are induced by the intrinsic asphericity of evolving structures and by the external tidal stresses exerted by the surrounding (inhomogeneous) large-scale matter distribution. These flows are a manifestation of the tidally induced anisotropic contraction of matter into planar and filamentary features, locked into a coherent pattern through highly dense compact clusters which form at the peaks in the primordial density field. It forms the basis for our understanding of the cosmic web (Bond et al. 1996), (also see van de Weygaert 2006).

The impression provided by the shear field in Fig. 14 is akin to that of the velocity divergence distribution (Fig. 11) and that of the density distribution (Fig. 5). Evidently there is a strong coupling between the density environment and the strength of the shear field. The velocity shear attains the highest values in and near high-density regions, while the large empty void regions are regions in which shear flows are hardly relevant with respect to the radial outflow (i.e. the velocity divergence amplitude). This is entirely in line with theoretical expectations (Hoffman 1986; Bertschinger & Jain 1994).

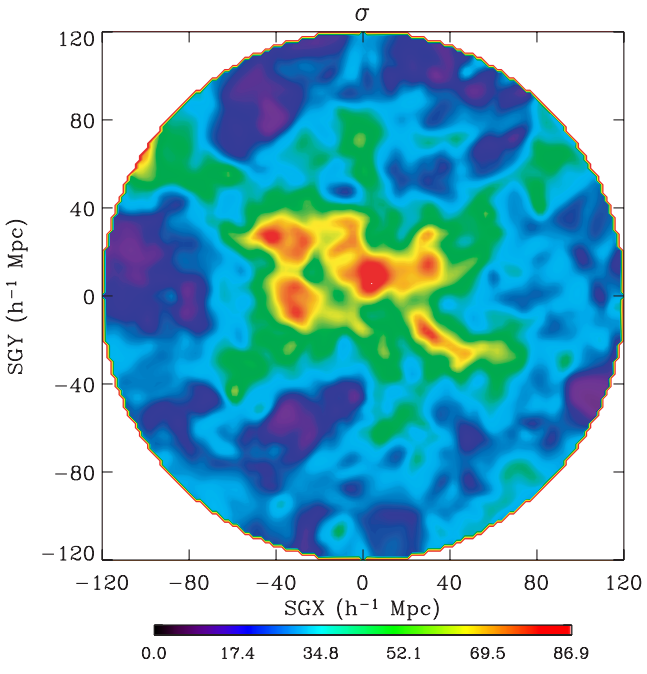

Figure 14. DTFE velocity shear field projected along the Z-supergalactic plane. The slice corresponds to the one presented in Fig. 5. We have plotted the velocity shear amplitude σ in units of the Hubble parameter. The colour bar indicates the values of the velocity shear in the colour contour map.

The spatial shear distribution suggests a very strong tidal force field in the central region of the local Universe, in the supergalactic *XY* plane. Most outstanding are the features in the supergalactic *XY* plane, in particular the ridge running through the central universe from the Pisces–Perseus supercluster towards the Shapley concentration. On one hand, this impression forms a telling manifestation of the characteristic quadrupolar pattern of the local mass distribution, defined by the Hydra–Centaurus supercluster (the GA region) and the Perseus supercluster region. Even though undoubtedly real this impression of a strong tidal field in the central region is partially biased by the effect of a considerably better spatial resolution in the central $30\,h^{-1}$ Mpc of our sample than in the outer regions and the resulting absence of the (stronger) higher frequency components present in the centre. In order to be able to assess the impact of this effect we compare the shear field maps for a smoothing radius of $3.8\,h^{-1}$ Mpc with those for $12\,h^{-1}$ Mpc in Fig. 15. While it confirms the tendency of higher shear values in the central region due to the resolved small-scale contributions, the $12\,h^{-1}$ Mpc convincingly delineates large-scale patterns responsible for considerable tidal stresses. The low-resolution, large-scale map does indeed demonstrate the reality of the prominent tidal features in the supergalactic (*XY*) plane. Its prominent dynamical role is additionally emphasized by the low-resolution *XZ* map where the plane stands out as the central edge marked by high shear values. Interesting features may also be observed in other regions of the sample volume: an interesting filamentary extension towards [SGY, SGZ] $\approx [-40, -100]\,h^{-1}$ Mpc can be observed in the *YZ* map.

10.1 The DTFE vorticity map

Vorticity is not expected to play any role of significance as a result of the 'linearized' origin of our PSCz velocities. The top-hat filter of $R_{\rm TH} = 5\,h^{-1}$ Mpc used to defined the velocity sample is an assurance for the linearity of practically all sample velocity data.

The presence of vorticity in our DTFE reconstructions should therefore provide us with a reasonably good impression of the influence of systematic artefacts in our maps. Regions populated with considerable large or abundant clusters (e.g. GA, Pisces–Perseus), do retain some measure of vorticity, even after smoothing. Also the DTFE method itself also introduces a small spurious vorticity component as a result of its linear interpolation scheme. A careful analysis of this artefact in our maps, and the effects for the DTFE velocity reconstruction, will be presented in Romano-Diaz, van de Weygaert & Schaap (in preparation).

11 SUMMARY AND DISCUSSION

The DTFE (see Schaap & van de Weygaert 2000) has been applied to a combined analysis of the density and velocity flow fields in the local Universe. The prime objective of this study has been the production of optimal resolution 3D maps of the volume-weighted velocity and density fields throughout the nearby universe, the basis for a detailed study of the structure and dynamics of the cosmic web at each level probed by underlying galaxy sample. In order

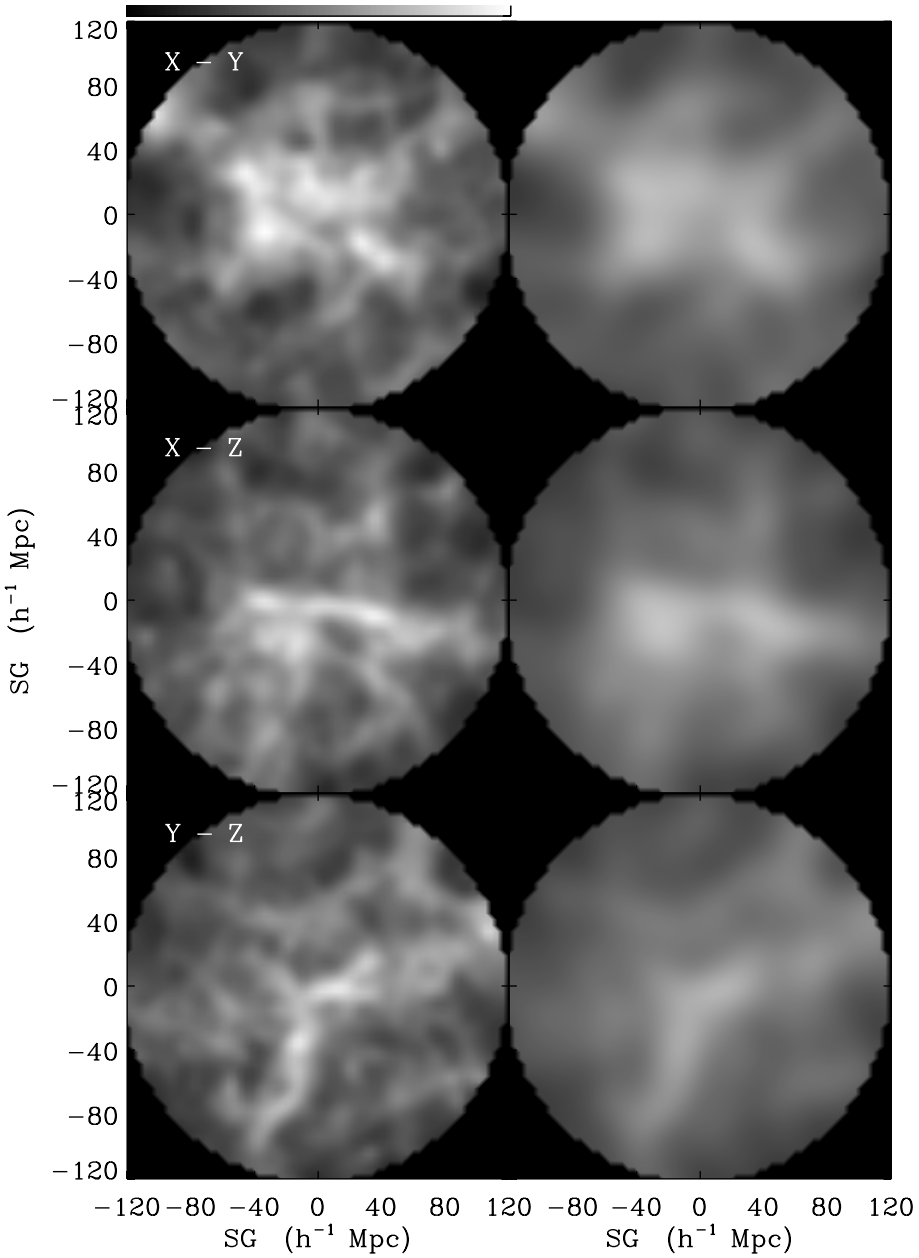

Figure 15. The DTFE velocity shear field on a smoothing scale of $3.8\,h^{-1}$ Mpc (left-hand column) and $10\,h^{-1}$ Mpc (right-hand column). The maps in the consecutive rows concern the three mutually perpendicular central supergalactic planes: the *XY*, *XZ* and *YZ* planes (from top to bottom). Note that the map on a scale of $3.8\,h^{-1}$ Mpc is uniform only out to a radius of $30\,h^{-1}$ Mpc, with a gradually diminishing resolution towards the outer edge of the sample volume. Also compare the images with the density fields in Figs 8 and 9. The grey-scale values are in units of the Hubble parameter H_0, with their values given in the bar at the top of the figure.

to have a reasonably complete sample of galaxy peculiar velocities throughout the surrounding local Universe we used the PSC*z* galaxy redshift catalogue translated into galaxy positions and velocities by means of the method I linearization process of Branchini et al. (1999).

The spatial galaxy distribution of the PSC*z* catalogue defines a Voronoi and Delaunay tessellation. These epitomize the most pure locally defined division of space in the PSC*z* volume. The self-adaptive nature of the Voronoi/Delaunay tessellations concerns both spatial resolution and local geometry. The high-level sensitivity to the local point distribution is exploited by DTFE (Schaap & van de Weygaert 2000) to produce an estimate of the local density at each sample point. The Delaunay tessellation is subsequently used as adaptive multidimensional spatial interpolation grid. The construction of the Voronoi and Delaunay tessellation is the most demanding task of the DTFE routine. Once this has been accomplished, they can be used for both the density and velocity fields (and basically any relevant field).

Because DTFE is based upon linear interpolation and involves constant field gradients within each Delaunay tetrahedron, the analysis of the cosmic velocity field automatically yields maps of the velocity divergence, shear and even vorticity. The spatial distribution of these quantities in DTFE is marked by a discontinuous zeroth-order map marked by Delaunay regions in which divergence,

shear or vorticity has a constant value. To sensibly relate the DTFE velocity divergence and shear fields it is necessary to smooth over a scale comparable to that of the corresponding Delaunay cells.

Earlier studies (Schaap & van de Weygaert 2007) have made clear that DTFE is particularly optimized for the analysis of mass distributions marked by one or more of the essential aspects of the non-linear cosmic web of the Mpc universe (Bond et al. 1996). One of the main advantages of DTFE is its large dynamic range, allowing it to trace small-scale structures along with the large-scale environment in which they are embedded. The spatial and morphological adaptivity of DTFE is ideally suited for dissecting the essential components of the non-linear web-like cosmic matter distribution. It resolves a hierarchically structured matter distribution to the smallest possible resolution scale set by the particle number density. Perhaps most outstanding is the ability of DTFE to retain the morphology, i.e. shape of the features and patterns in the matter distribution: the characteristic anisotropic filamentary and planar features of the *cosmic web* are fully reproduced in the continuous DTFE density field (Schaap & van de Weygaert 2000). Also the third major characteristic of the non-linear Mpc universe, the dominant existence of near-empty voids, is resolved by DTFE. Both their flat internal density distribution and their sharp outline and boundary are recovered in detail, while shot-noise in these sparsely sampled regions tends to be suppressed.

The maps of the PSCz local Universe reveal a sharply defined density field in which many familiar structures and features can be recognized at an optimal spatial resolution. The region around the Local Group and its filamentary extension towards the Hydra–Centaurus and Shapley complexes as well as the Pisces–Perseus supercluster are prominently resolved in the DTFE density fields. Moreover, these features are as clearly and sharply defined in the corresponding velocity flows. Perhaps the most outstanding features in the velocity vector fields are the radially expanding void regions. In comparison to earlier published maps of the density field and velocity flow in the PSCz sample volume (Branchini et al. 1999; Schmoldt et al. 1999) the DTFE maps have a considerably sharper defined appearance. While conventional maps suppressed small-scale details and were at loss in undersampled void regions, in particular with respect to the interpolation of the velocity field, the DTFE fields reveal a beautifully textured flow field. The DTFE flows are marked by prominent bulk flows, shear flows and radial inflow (Coma cluster). Arguably the most outstanding and unique feature of the DTFE maps is the sharply defined radial outflow regions in and around underdense voids, marking the dynamical importance of voids in the local Universe.

The present study includes two specific aspects and challenges for DTFE: (1) the application of DTFE to reconstruct the density field as well as the corresponding velocity field in the same cosmic volume and (2) the gradually diminishing spatial resolution as a function of radial distance as a consequence of the flux-limited nature of the PSCz sample.

While one may correct estimated density values by taking into account the well-defined radial selection function, it is not possible to correct for the loss in spatial resolution: the lower galaxy sampling density goes along with a loss, at increasing distances, in spectral coverage of the maps. A full recovery would have to involve preconceived notions on the cosmological structure formation scenario, i.e. the power spectrum. The relatively prominent central values in the density, velocity divergence and shear maps are a reflection of this effect. On the other hand, the velocity field itself – less affected by the lack of high-frequency spectral power at large distances – for all practical purposes appears to be uniformly covered by the DTFE reconstruction. The sharply outlined edges of superclusters and the radial outflow of voids are found throughout the PSCz volume.

We have addressed the relationship between the density field and velocity field by correlating the density values with the local velocity divergence and shear. Overall, the linear density–velocity divergence relationship is accurately reproduced. This reflects the origin of the galaxy velocities, having been computed from a redshift map through a linearization procedure. These simple quantitative relations do not express the spatial coherence and correlations within the velocity field. The tight spatial correspondence between density features and velocity flows in the DTFE maps – voids with radial outflow, elongated and flattened superclusters with bulk and shear flows – does demonstrate the remarkable adaptive nature of the DTFE technique and its promise of understanding the dynamics of the cosmic web. The maximum expansion rate of voids defines a sharp cut-off in the velocity divergence PDF. It enabled us to test the self-consistency of the DTFE method. Indeed it confirmed the value of $\Omega_{\rm m} \approx 0.35$ of the cosmology underlying the galaxy velocity data.

For furthering our insight into the velocity field in the nearby universe it would be desirable to be able to probe quasi-linear contributions to the velocity field. Techniques like the FAM-z of Branchini, Eldar & Nusser (2002), applied in combination with the DTFE algorithm, would offer a potentially promising approach. While this study has shown the potential of DTFE towards a successful analysis of velocity fields it concerns a test on the basis of a sample of preprocessed galaxy velocities. This includes the assumption that the velocity field linearization (Branchini et al. 1999) has successfully dealt with redshift-space distortions and sampling effects.

Ultimately we will seek to develop a DTFE-based formalism to directly analyse samples of galaxy peculiar velocities on the basis of the 'raw' observational data. The challenge is found in a few aspects. One aspect concerns errors and sampling effects. A second aspect involves redshift distortions. A third complicating aspect involves fundamental assumptions behind the velocity field reconstruction procedure, such as the requirement of laminarity of the flow. An extensive study of various sampling effects, such as decreased sampling density and inhomogeneous sampling, on simulation-based data do show that the noise level of the DTFE velocity reconstructions does increase but that this does not involve any systematic shifts (Romano-Díaz 2004). Given the acclaimed optimal triangulation properties of Delaunay grids underlying the development of DTFE this may not come as a surprise. The same study involved tests of the effects of a variety of different error contributions. They induced similar effects as a less balanced galaxy sampling. These results will be presented in an extensive study and report on error and sampling effects in a forthcoming paper. More challenging issues concern the physically more profound aspects of redshift distortions and higher order flow characteristics. As a first-order version of the wider class of natural neighbour interpolation schemes (Sibson 1980, 1981; Watson 1992), DTFE may be extended to a higher order natural neighbour interpolation scheme based upon the Delaunay tessellation of a galaxy sample. Such a formalism would enable a more complex treatment of non-linear velocity flows, possibly even of multistream flows. Already we have been working towards the implementation of these higher order interpolation schemes (see van de Weygaert & Schaap 2007, for a review on the basics), and we plan to look into the possibility on the basis of routines made available through CGAL.[7] On the other hand, highly

[7] CGAL is a c^{++} library of algorithms and data structures for Computational Geometry, see www.cgal.org.

mixed virialized regions will remain beyond the scope of these interpolation techniques. This may hardly be considered a constraint given the fact that for the foreseeable future the focus of nearly all galaxy peculiar velocity surveys will be the dynamics of large-scale structures. The inversion from redshift- to real-space data may be facilitated and enabled by using the virtues of a Delaunay grid for the solution of PDEs. The use of Delaunay tessellations as grids for the numerical solution of PDEs has been first described by Braun & Sambridge (1995), their success provides substantial imperative for the formulation of the redshift- to real-space inversion following these lines.

In the meantime DTFE has been elaborated upon through the development of a number of specific feature detecting techniques. The Multiscale Morphology Filter (MMF; Aragon et al. 2007) forms a highly promising tool for selection and identification of filamentary and planar structures and their spatial relationship with neighbouring structures. The watershed-based void-detection algorithm developed by Platen et al. (2007) has been applied towards the analysis of the hierarchical evolution of voids (see Sheth & van de Weygaert 2004). In all cases, the fully adaptive and optimal tessellation based characteristics of DTFE form the crucial starting point.

ACKNOWLEDGMENTS

We are very grateful to E. Branchini for providing us with the PSC*z* sample of galaxy positions and linearized velocities. Also we wish to thank W. Schaap for the use of DTFE routines and for useful comments and F. Bernardeau for crucial advice. We greatly benefited from discussions about velocity fields and Delaunay tessellations with Bernard Jones and Manolis Plionis. Finally, we wish to thank the referee, E. Branchini, for useful suggestions and comments. ERD has been supported by the Golda Meier Fellowship at the Hebrew University, and HST/AR 10976, NASA/LTSA 5-13063, NSF/AST 02-06251 and NASA/ATP NNG06-GJ35G. Part of this work was finished while enjoying the hospitality of the NOA in Athens, which we gratefully acknowledge.

REFERENCES

Arad I., Dekel A., Klypin A., 2004, MNRAS, 353, 15
Aragón-Calvo M., Jones B. J. T., van de Weygaert R., van der Hulst J. M. 2007, A&A, submitted
Ascasibar Y., Binney J., 2005, MNRAS, 356, 872
Baker J. E., Davis M., Strauss M. A., Lahav O., Santiago B. X., 1998, ApJ, 508, 6
Basilakos S., Plionis M., 1998, MNRAS, 299, 637
Bernardeau F., 1992, ApJ, 390, L61
Bernardeau F., 1994, ApJ, 433, 1
Bernardeau F., Kofman L., 1995, ApJ, 443, 479
Bernardeau F., van de Weygaert R., 1996, MNRAS, 279, 693
Bernardeau F., Juszkiewicz R., Dekel A., Bouchet F. R., 1995, MNRAS, 274, 20
Bernardeau F., van de Weygaert R., Hivon E., Bouchet F., 1997, MNRAS, 290, 566
Bernardeau F., Colombi S., Gaztanaga E., Scoccimarro R., 2002, Phys. Rep., 367, 1
Bertschinger E., 1987, ApJ, 323, L103
Bertschinger E., Jain B., 1994, ApJ, 431, 486
Bertschinger E., Dekel A., Faber S. M., Dressler A., Burstein D., 1990, ApJ, 364, 370
Bond J. R., Kofman L., Pogosyan D., 1996, Nat, 380, 603
Bradač M., Schneider P., Lombardi M., Steinmetz M., Koopmans L. V. E., Navarro J. F., 2004, A&A, 423, 797
Branchini E. et al., 1999, MNRAS, 308, 1
Branchini E. et al., 2001, MNRAS, 326, 1191
Branchini E., Eldar A., Nusser A., 2002, MNRAS, 335, 53
Braun J., Sambridge M., 1995, Nat, 376, 660
Brown G. S., 1965, N.Z. Forestry Serv. Res. Notes, 38, 1
Dekel A., 1994, ARA&A, 32, 371
Dekel A., Rees M. J., 1994, ApJ, 422, L1
Dekel A., Eldar A., Kolatt T., Yahil A., Willick J. A., Faber S. M., Courteau S., Burstein D., 1999, ApJ, 522, 1
Delaunay B. N., 1934, Bull. Acad. Sci. USSR: Clase Sci. Mater., 7, 793
Ebeling H., Wiedenmann G., 1993, Phys. Rev. E, 47, 704
Erdoğdu P. et al., 2006, MNRAS, 368, 1515
Fisher K. B., Huchra J. P., Strauss M. A., Davis M., Yahil A., Schlegel D., 1995, ApJS, 100, 69
Hockney R. W., Eastwood J. W., 1988, Computer Simulation Using Particles. Hilger, Bristol
Hoffman Y., 1986, ApJ, 308, 493
Hoffman Y., Ribak E., 1991, ApJ, 380, L5
Icke V., 1984, MNRAS, 206, 1P
Juszkiewicz R., Weinberg D. H., Amsterdamski P., Chodorowski M., Bouchet F., 1995, ApJ, 442, 39
Kim R. S. J. et al., 2002, AJ, 123, 20
Kocevski D. D., Ebeling H., 2006, ApJ, 645, 1043
Li G.-L., Mao S., Jing Y. P., Kang X., Bartelmann M., 2006, ApJ, 652, 43
Lilje P. B., Yahil A., Jones B. J. T., 1986, ApJ, 307, 91
Łokas E. L., Juszkiewicz R., Weinberg D. H., Bouchet F. R., 1995, MNRAS, 274, 730
Lopes P. A. A., de Carvalho R. R., Gal R. R., Djorgovski S. G., Odewahn S. C., Mahabal A. A., Brunner R. J., 2004, AJ, 128, 1017
Marinoni C., Davis M., Newman J. A., Coil A. L., 2002, ApJ, 580, 122
Martínez V. J., Starck J.-L., Saar E., Donoho D. L., Reynolds S. C., de la Cruz P., Paredes S., 2005, ApJ, 634, 744
Neyrinck M. C., Gnedin N. Y., Hamilton A. J. S., 2005, MNRAS, 356, 1222
Nusser A., Dekel A., Bertschinger E., Blumenthal G. R., 1991, ApJ, 379, 6
Okabe A., Boots B., Sugihara K., Chiu S. N., 2000, Spatial Tessellations: Concepts and Applications of Voronoi Diagrams, 2nd edn. Wiley, Chichester, Toronto
Ord J. K., 1978, Math. Sci., 3, 23
Peebles P. J. E., 1980, The Large-Scale Structure of the Universe. Princeton Univ. Press, Princeton, NJ
Platen E., van de Weygaert R., Jones B. J. T., 2007, MNRAS, 380, 551
Plionis M., Basilakos S., 2002, MNRAS, 330, 399
Plionis M., Kolokotronis V., 1998, ApJ, 500, 1
Ramella M., Boschin W., Fadda D., Nonino M., 2001, A&A, 368, 776
Romano-Díaz E., 2004, PhD thesis, Rijksuniversiteit Groningen
Rowan-Robinson M. et al., 2000, MNRAS, 314, 375
Sambridge M., 1999, Geophys. J. Int., 138, 479
Sambridge M., Braun J., McQueen H., 1995, Geophys. J. Int., 122, 837
Saunders W. et al., 2000, MNRAS, 317, 55
Schaap W. E., 2006, PhD thesis, Rijksuniversiteit Groningen
Schaap W. E., van de Weygaert R., 2000, A&A, 363, L29
Schaap W. E., van de Weygaert R., 2003, in Babu G. J, Feigelson E. D., eds, Statistical Challenges in Modern Astronomy III. Springer, New York
Schaap W. E., van de Weygaert R. 2007, A&A, submitted
Schmoldt I. M. et al., 1999, AJ, 118, 1146
Sheth R. K., van de Weygaert R., 2004, MNRAS, 350, 517
Sibson R., 1980, Math. Proc. Cambridge Phil. Soc., 87, 151
Sibson R., 1981, in Barnet V., ed., Interpreting Multi-variate Data. Wiley, Chichester, p. 21
Strauss M. A., Willick J. A., 1995, Phys. Rep., 261, 271
Sukumar N., 1998, PhD thesis, Northwestern Univ.
Suto Y., Fujita M., 1990, ApJ, 360, 7
Teodoro L., Branchini E., Frenk C., 2003, preprint (astro-ph/0308027)
van de Weygaert R., 1991, PhD thesis, Rijksuniversiteit Leiden
van de Weygaert R., 1994, A&A, 283, 361
van de Weygaert R., 2002, in Plionis M., Cotsakis S., eds, ASSL 276, Proc. 2nd Hellenic Cosmology Meeting: Modern Theoretical and Observational Cosmology. Kluwer, Dordrecht, p. 119

van de Weygaert R., 2006, in den Herder J. W., Yamasaki N., eds, Proc. Workshop Shonan Village Center, Measuring the Diffuse Intergalactic Medium. SRON, Utrecht
van de Weygaert R., Bertschinger E., 1996, MNRAS, 281, 84
van de Weygaert R., Schaap W., 2007, in Martínez V., Saar E., eds, Lecture Notes Summer School Valencia, Data Analysis in Cosmology. Springer-Verlag, New York, p. 128
Voronoi G., 1908, J. Reine Angew. Math., 134, 167
Watson D. F., 1992, Contouring: A Guide to the Analysis and Display of Spatial Data. Pergamom, Oxford
Willick J. A., Courteau S., Faber S. M., Burstein D., Dekel A., Strauss M. A., 1997, ApJS, 109, 333
Yahil A., Strauss M. A., Davis M., Huchra J. P., 1991, ApJ, 372, 380
Zaroubi S., Branchini E., Hoffman Y., da Costa L. N., 2002, MNRAS, 336, 1234
Zel'dovich Ya. B., 1970, A&A, 5, 84

This paper has been typeset from a TEX/LATEX file prepared by the author.